SANDIA REPORT
SAND2008-5999
Unlimited Release
Printed September 2008

Development of Nanostructured and Surface Modified Semiconductors for Hybrid Organic-Inorganic Solar Cells

Julia W.P. Hsu

Prepared by
Sandia National Laboratories
Albuquerque, New Mexico 87185 and Livermore, California 94550

Sandia is a multiprogram laboratory operated by Sandia Corporation,
a Lockheed Martin Company, for the United States Department of Energy's
National Nuclear Security Administration under Contract DE-AC04-94AL85000.

Issued by Sandia National Laboratories, operated for the United States Department of Energy by Sandia Corporation.

Available to DOE and DOE contractors from

U.S. Department of Energy
Office of Scientific and Technical Information
P.O. Box 62
Oak Ridge, TN 37831

Telephone: (865) 576-8401
Facsimile: (865) 576-5728
E-Mail: reports@adonis.osti.gov
Online ordering: http://www.osti.gov/bridge

Available to the public from

U.S. Department of Commerce
National Technical Information Service
5285 Port Royal Rd.
Springfield, VA 22161

Telephone: (800) 553-6847
Facsimile: (703) 605-6900
E-Mail: orders@ntis.fedworld.gov
Online order: http://www.ntis.gov/help/ordermethods.asp?loc=7-4-0#online

SAND2008-5999
Unlimited Release
Printed September 2008

Development of Nanostructured and Surface Modified Semiconductors for Hybrid Organic-Inorganic Solar Cells

Julia W. P. Hsu
Surface & Interface Scienes, Sandia National Laboratories
P. O. Box 5800 MS-1415, Albuquerque, NM 87185

ABSTRACT

Solar energy conversion is increasingly being recognized as one of the principal ways to meet future energy needs without causing detrimental environmental impact. Hybrid organic-inorganic solar cells (SCs) are attracting particular interest due to the potential for low cost manufacturing and for use in new applications, such as consumer electronics, architectural integration and light-weight sensors. Key materials advantages of these next generation SCs over conventional semiconductor SCs are in design opportunities – since the different functions of the SCs are carried out by different materials, there are greater materials choices for producing optimized structures. In this project, we explore the hybrid organic-inorganic solar cell system that consists of oxide, primarily ZnO, nanostructures as the electron transporter and poly-(3-hexylthiophene) (P3HT) as the light-absorber and hole transporter. It builds on our capabilities in the solution synthesis of nanostructured semiconducting oxide arrays to this photovoltaic (PV) technology. The three challenges in this hybrid material system for solar applications are (1) achieving inorganic nanostructures with critical spacing that matches the exciton diffusion in the polymer, ~ 10 nm, (2) infiltrating the polymer completely into the dense nanostructure arrays, and (3) optimizing the interfacial properties to facilitate efficient charge transfer. We have gained an understanding and control over growing oriented ZnO nanorods with sub-50 nm diameters and the required rod-to-rod spacing on various substrates. We have developed novel approaches to infiltrate commercially available P3HT in the narrow spacing between ZnO nanorods. Also, we have begun to explore ways to modify the interfacial properties. In addition, we have established device fabrication and testing capabilities at Sandia for prototype devices. Moreoever, the control synthesis of ZnO nanorod arrays lead to the development of an efficient anti-reflection coating for multicrystalline Si solar cells.

An important component of this project is the collaboration with Dr. Dave Ginley's group at NREL. The NREL efforts, which are funded by NREL's LDRD program, focus on measuring device performance, external quantum efficiency, photoconductance through highly specialized non-contact time-resolved microwave conductivity (TRMC) measurements, and vapor phase deposition of oxide materials. The close collaboration with NREL enables us to enter this competitive field in such short time. Joint publications and presentations have resulted from this fruitful collaboration. To this date, 5 referred journal papers have resulted from this project, with 2 more in preparation. Several invited talks and numerous contributed presentations in international conferences are also noted. Sandia has gained the reputation of being one of forefront research groups on nanostructured hybrid solar cells.

ACKNOWLEDGEMENTS

Y.-J. Lee, D. C. Olson, and J. A. Voigt made invaluable contributions to this project. In addition, we would like to acknowledge T. L. Sounart (Intel), J. Liu (PNNL) and E. D. Spoerke for their work in nanocrystal growth, D. A. Scrymgeour on atomic force microscopy characterization, B. McKenzie for scanning electron microscopy imaging, E. Fang and M. Piech for ZnO nanorod synthesis, D. R. Tallant and R. Simpson for photoluminescence spectroscopy, N. Bell for calculating the speciation diagrams, D. S. Ruby and J. Finn for antireflectance measurements, D. W. Peters for rigorous coupled wave analysis, N. A. Chang for her initial work on polymer infiltration. Further more, we thank our collaborators at NREL: M. S. White, N. Kopidakis, S. E. Shaheen, and D. S. Ginley. This work is supported by the Sandia National Laboratories (SNL) Laboratory-Directed Research and Development Program (LDRD). SNL is a multi program laboratory operated by Sandia Corporation, a Lockheed Martin Company, for the Department of Energy under Contract DE-AC04-94AL85000.

CONTENTS

Control of ZnO Nanorod Array Alignment Synthesized Via Seeded Solution Growth

Introduction

Hybrid polymer-inorganic photovoltaic (PV) devices, consisting of a hole transporting conjugated polymer and an electron transporting inorganic material in close contact, represent a promising opportunity for fabricating low cost, large area solar cells. When all processing steps are conducted at or near room temperature, it may be possible to integrate the PV fabrication with flexible plastic substrates [1], further reducing cost and enabling novel applications. Current hybrid PV devices utilize a variety of electron transporting materials, including fullerene derivatives [2,3], chalcogenide nanorods [4], and oxide nanoparticles [5] and extended nanostructures [6], with a current maximum solar polar conversion efficiency of 4.4% [3]. Compared to the alternatives, oxides have the advantages of better thermal and environmental stability, tunable band structures, and higher electron mobilities. In particular, highly aligned ZnO nanorod arrays (NRAs) can be grown at low temperature in dilute aqueous solutions and may serve as the electron transporter in conjugated polymer-oxide hybrid PV devices due to low fabrication cost, high surface area, and opportunities for bandgap engineering. Ultrafast photoinduced charge transfer has been shown to occur between a conjugated polymer and ZnO [7]. ZnO thin films also exhibited a high electron mobility of up to 100 $cm^2\ V^{-1}\ s^{-1}$ [8]. Moreover, a wide variety of ZnO nanostructures with high surface areas and controlled spacing have been demonstrated. Based on the work of Vayssieres et al. [9], aligned ZnO NRAs have been synthesized via solution decomposition of Zn^{2+} complexes [10-13], and have been utilized as the electron transport layer in dye-sensitized [14] and hybrid polymer-ZnO [15] PV devices.

Recently, Greene et al. reported a two-step method consisting of seeding and subsequent aqueous rod growth to produce dense ZnO NRAs for PV applications [12]. Using this method, ZnO NRAs were synthesized with excellent vertical alignment, as indicated by the absence of all ZnO peaks other than (002) in x-ray diffraction (XRD) data. Such highly aligned NRAs may potentially improve the performance of PV devices due to increased packing density and interfacial area, as well as improved conjugated polymer crystallinity and carrier transport due to preferential alignment of the polymer along a ZnO facet [16]. However, the effects of certain seeding and growth parameters on the resulting structure and properties of the ZnO NRAs have not been systematically studied. Here, we present experimental data showing that the ZnO nanorod alignment, density, and size depend on the seeding conditions, specifically the ambient humidity level during seeding and the substrate roughness.

Experimental Procedure

Zinc acetate dihydrate (99.999%, Aldrich), zinc nitrate hexahydrate (Fisher), and methenamine (Fisher) were used as received. The ZnO NRAs were synthesized using a procedure based on a previous report [12]. Five mM solution of zinc acetate dehydrate in ethanol was made by stirring at 60 °C for 1 hour. 2.5 cm x 1.25 cm pieces of *N*-type Si(100) were used for the seeding relative humidity (RH) study, and fluorine doped tin oxide (FTO) on glass (TEC, Pilkington) and indium tin oxide on glass (Delta Technologies) with various conducting oxide thicknesses were used for the substrate roughness study. All substrates were cleaned by sonicating in methylene chloride

(10 min) and then in acetone (10 min), rinsing with methanol, and UV ozone treatment (UVO-Cleaner, Jelight) for 20 min. The seeding process was carried out at room temperature (23 °C) in a constant humidity plastic glove box. The RH level was controlled to +/- 3% by blowing a reservoir of water with dry N_2 (g), and was measured with a digital hygrometer/thermometer (Mannix). Each substrate was cleaned with a blast of N_2 (g) immediately prior to depositing 15 μL of the 5 mM zinc acetate solution on the center of the substrate. The solution spread to cover the entire substrate, and was allowed to evaporate for 25 s before the substrate was rinsed with a copious amount of ethanol. The zinc acetate coating procedure was repeated four additional times, and the substrate was placed in a box furnace (Lindberg) at 350 °C for 20 min to anneal the seeds. The entire seeding step was repeated one additional time to ensure complete substrate coverage with ZnO seeds in accordance with the previous report [12], although we subsequently discovered that the repetition was not necessary if the seeding RH was well controlled. Twelve mL of the growth solution containing 25 mM zinc nitrate and 25 mM methenamine in water was pipetted in a 20 mL glass scintillation vial (VWR), and the substrate was placed at a ~ 30° angle to horizontal in the vial. Each vial was placed in an oven (Lindberg) at 92.5 °C for 120 min for the nanorod growth. Finally, each substrate was removed from the vial, rinsed with water to remove loose ZnO precipitates, and dried in air.

The morphology of the ZnO NRAs was characterized by a Zeiss field-emission source scanning electron microscope (SEM). X-ray diffraction (XRD) spectra for $2\theta = 30°$ to 65° with a step size of 0.04° using Cu Kα radiation were collected with a thin film diffractometer operating at 40 kV and 30 mA (Rigaku). Visible photoluminescence (PL) microscopy and spectroscopy were performed on an Olympus BX51 microscope with Hg illumination and UV filter cube (U-MWU2, excitation = 330-385 nm, emission ≥ 420 nm), using a 150x objective (0.9 NA, LMPlanApo) and an integration time of 20 s on a charged coupled device (CCD) camera. UV-visible PL spectra were measured on a customized spectrometer using xenon lamp excitation passed through a double monochromator and a 7-54 filter, resulting in a center wavelength of 350 nm. PL spectra were collected by a lens/fiber optic system coupled to a 0.6 m spectrograph with a CCD detector, with a sampling area of ~ 3 mm x 0.5 mm. Tapping mode atomic force microscopy (AFM) images of the seed layer were performed with a scan area of 5 μm x 5 μm (Digital Instrument 3100). The PL spectra were normalized to ZnO nanorod length measured by SEM, in order to clarify the effect of NRA morphology and density on PL intensity. Static contact angles of water on the seed layer were measured with a commercial apparatus (Kruss).

Results and Discussion

The humidity level during seeding strongly influenced the alignment, density, and nanorod size of the ZnO NRAs, as shown by the SEM images (Fig. 1). When the substrates were seeded at 8% RH, a relatively sparse and poorly alignment ZnO NRA was synthesized, with an average rod diameter and length of 80 nm and 850 nm, respectively (Fig. 1a). In addition, from the SEM cross section, multiple ZnO nanorods appear to originate from the same point on the substrate, suggesting that a single seed may be responsible for the growth of multiple rods. It should also be noted that the ZnO NRAs grown from substrates seeded at 8% RH has a high variation in morphology from experiment to experiment. For example, poorly aligned ZnO nanorods with diameter of 140 nm were synthesized in another experiment with the same conditions, similar to results observed when ZnO nanoparticles were used as the seed layer [10]. In contrast, ZnO

nanorods synthesized on substrates seeded at 32% RH and 60% RH were densely packed and well aligned, with an average rod diameter and length of 50 nm and 550 nm, respectively (Fig. 1b and 1c). The higher areal density of the nanorods resulted in the shorter length of the highly aligned NRAs. In SEM cross sections, the great majority of ZnO nanorods grew from individual points on the substrate, unlike the 8% RH sample. We found the threshold for the conversion between the two types of NRA morphology to be ~ 20% RH. On the other hand, when the seeding humidity level is above 60%, nanorods with large diameters (> 100 nm) appear with greater frequency among the normal sized rods. For example, Fig. 1c, top shows a greater polydispersity in nanorod diameter in the 60% RH sample compared with the more uniform diameter in the 32% RH sample (Fig. 1b, top). Such large diameter features may correspond to the fusion of multiple ZnO nanorods, which is visible in the cross sections (Fig. 1b and 1c).

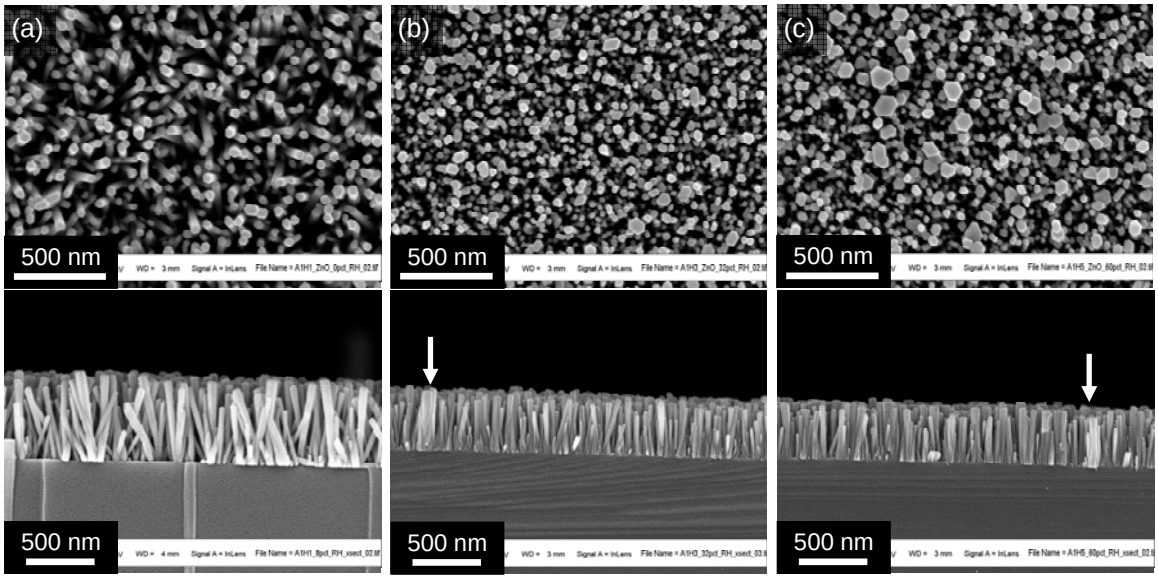

Fig. 1. Plane view (top) and cross section (bottom) SEM of ZnO nanorods arrays with the seeding process done at (a) 8% RH, (b) 32% RH, and (c) 60% RH. Arrows indicate larger diameter fused nanorods.

XRD spectra (Fig. 2) and PL studies (Fig. 3) of these ZnO NRAs further quantify the observations obtained from the SEM data. For example, only the ZnO NRA seeded at 8% RH exhibited non-(002) XRD peaks (Fig. 2), signifying a misalignment of the rods with respect to the sample normal. It should be noted that even for such a "disordered" rod array, the (103) peak intensity is only 2.5% that of the (002) peak, suggesting that the nanorods are still reasonably well aligned compared to results from most other seeding methods [9-11]. In comparison, the NRAs seeded at RH values higher than ~ 20% exhibited only the (002) peak (Fig. 2). Consistent with SEM results, all NRAs seeded at humidity levels higher than this threshold are well aligned, with the [001] axis perpendicular to the substrates.

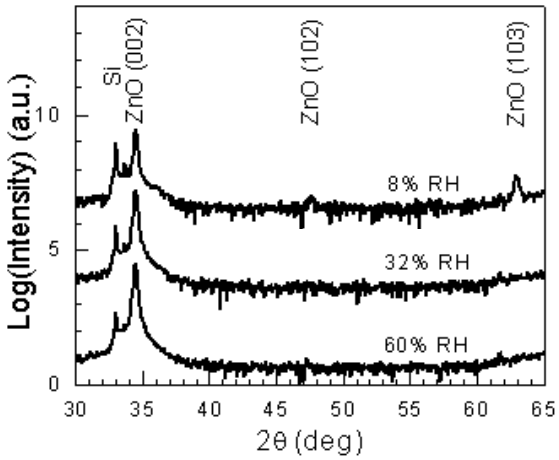

Fig. 2. XRD spectra of ZnO NRAs seeded at 8% RH, 32% RH, and 60% RH. The plots are offset for clarity.

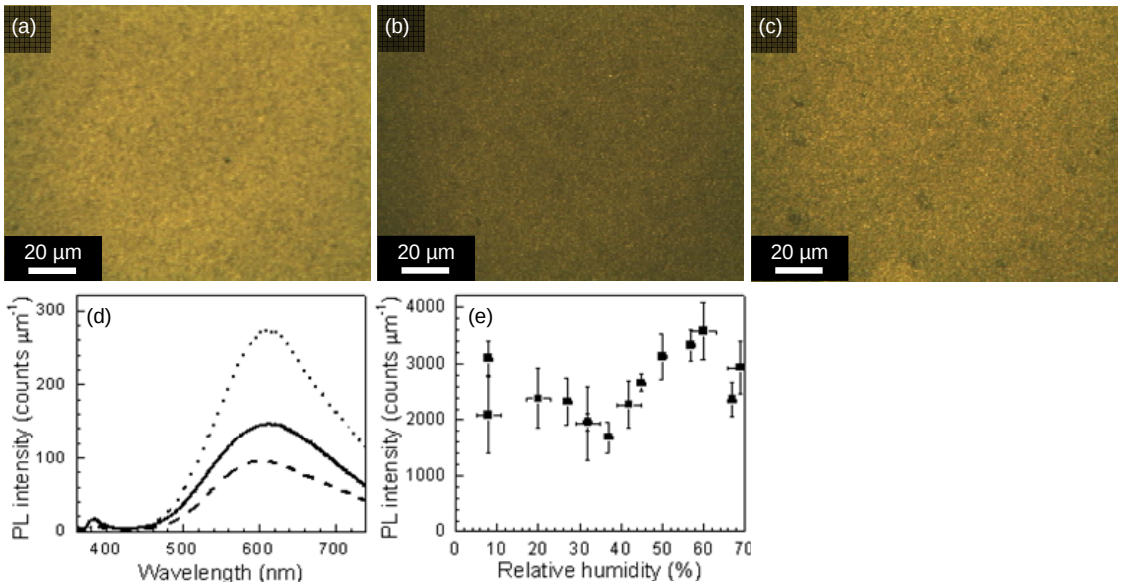

Fig. 3. PL micrographs of ZnO NRAs seeded at (a) 8% RH, (b) 32% RH, and (c) 60% RH. (d) PL spectra of ZnO NRA seeded at 8% RH (solid), 32% RH (dash), and 67% RH (dots). (e) Visible PL peak intensities of ZnO NRAs as a function of seeding RH level, showing decreased PL above a threshold of ~ 20% RH.

Figure 3 shows the PL micrographs and spectra of the ZnO NRAs. The yellow-orange deep-level luminescence is characteristic of solution-grown ZnO nanorods and has been associated with excess oxygen [11,13]. While the PL spectra from all samples exhibit the same profile (Fig. 3d), their overall PL intensities depend on the diameter of the nanorods. In particular, ZnO NRAs seeded at 30 – 40% RH (e.g. Fig. 3b) exhibited a lower visible PL intensity compared to the other samples. When the visible PL peak intensities of the ZnO NRAs were plotted as a function of the seeding RH value, we found that the intensity decreased as RH rose above a threshold of ~ 20% RH until a minimum was reached at ~ 35% RH, after which it began to increase with further rise in RH (Fig. 3e). These results may be explained by non-radiative recombination

processes at the nanorod surface. Thus, the high surface area to volume ratio of a smaller diameter NRA should lower PL. In addition, ZnO NRAs seeded at RH $\geq$ 60% exhibited distinct spatial variations in PL intensity (Fig. 3c), indicating that a high seeding humidity results in a greater variation in nanorod dimensions, in good agreement with the SEM result. In short, PL microscopy represents a quick, qualitative method to compare average rod diameters from different samples and evaluate the distribution of diameters within a ZnO NRA.

To understand the mechanism by which the humidity level during seeding affected the morphology of the ZnO NRAs, we examined the ZnO seed layers using AFM and contact angle measurement. Both experimental techniques indicated that substrates seeded at higher RH values contained a higher density of seeds compared to substrates seeded at lower RH values. For example, AFM of the seed layer formed at 8% RH showed a low density layer of isolated seeds on the substrate (Fig. 4a). Such low seed density is consistent with the growth of multiple rods from a single seed observed in SEM (Fig. 1a). In contrast, seed layers formed at 32% RH and 60% RH exhibited a continuous layer with a high density of seeds (Fig. 4b and 4c). In other words, the higher humidity level is responsible for increasing the areal density of the ZnO seeds, which acted as nucleation sites for the growth of ZnO nanorods. The static contact angle of water on the seed layers and the rms roughness valued derived from the AFM data also shows the effect of humidity on the seeding process (Table 1). At 8% RH, the seeded substrate exhibited a slightly higher contact angle and a similar rms roughness compared to a bare Si substrate, indicating low surface coverage by the seeds. As the seeding relative humidity increased, the contact angle and rms roughness also increased, to maximum values of 26º and 2.19 nm, respectively, at 60% RH, suggesting that significantly more seed material is formed at high ambient humidity levels. Based on these results, we believe that ambient water vapor is necessary to hydrolyze the seed layer to form products that are insoluble during the subsequent ethanol rinse. These products remain on the substrate and are converted to ZnO during the annealing step to serve as nucleation sites for the ZnO nanorods during the growth step. The proposed reaction scheme is shown in Equation 1.

$$\begin{aligned} &Zn(CH_3COO)_2 + 2H_2O \longrightarrow Zn(OH)_2 + 2CH_3COOH \\ &Zn(OH)_2 \xrightarrow{\Delta} ZnO + H_2O\uparrow \end{aligned} \qquad (1)$$

To test this hypothesis, we added water (1% by volume) to a 5 mM zinc acetate solution in ethanol, and found that the solution almost immediately became cloudy due to light scattering from the hydrolysis products. Thus, through careful control of the seeding RH level, the density of seeds on the substrate can be varied, which in turn affects the alignment, density, and size of the resulting NRA.

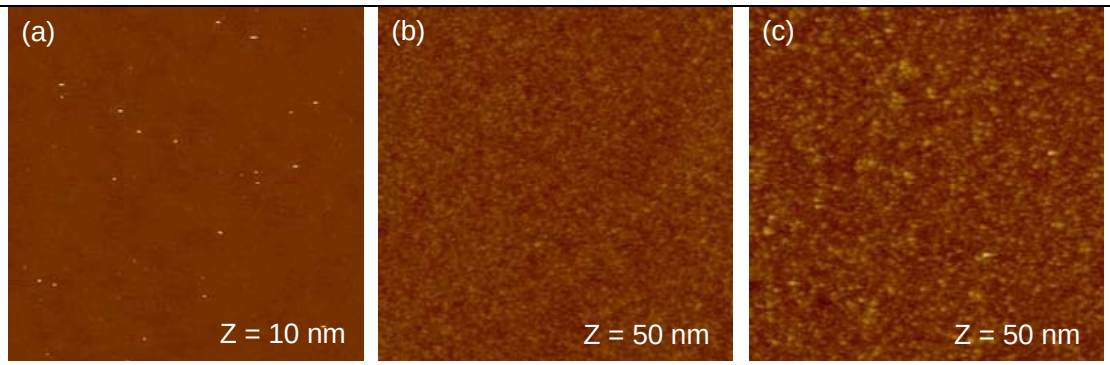

Fig. 4. AFM scans of ZnO seed layers seeded at (a) 8% RH, (b) 32% RH, and (c) 60% RH. The lateral scan dimensions are 5 μm x 5 μm, and the Z value denotes the full vertical length scale.

RH (%)	Contact angle (deg)	Roughness (nm)
8	11 ± 2	0.17 ± 0.03
32	24 ± 1	1.44 ± 0.05
60	26 ± 1	2.19 ± 0.18
Bare Si	< 10	0.18 ± 0.07

Table 1. Static contact angle of water and rms roughness of ZnO seed layers seeded at various RH values and of a Si wafer after ozone treatment.

For PV applications, ZnO nanorods are commonly grown on transparent conducting oxides (TCOs) on glass. Two commonly used TCOs for PV are indium tin oxide (ITO) and fluorine doped tin oxide (FTO). For these TCOs, an increase in film thickness improves conductivity but also increases roughness. We examined the effect of the TCO substrate roughness on the alignment of ZnO NRAs, using a seeding humidity level of 32% RH. Figure 5 shows top-view SEM images of ZnO nanorods grown on TCO substrates with different FTO thicknesses. We found that the ZnO NRA became progressively less well aligned as the substrate rms roughness (as measured by AFM) increased (Fig. 5). The XRD spectra show that non-(002) peaks were already present even for the smoothest FTO substrate (rms roughness = 8.14 nm), and became more significant as the substrate roughness increased (Fig. 5a). For example, the intensity ratio of the (103) peak to the (002) peak for the ZnO rods grown on the smoothest FTO substrate equaled 0.018, or almost as high as the intensity ratio for the ZnO NRA seeded at 8% RH (0.025). As the substrate roughness approached 50 nm, the normalized peak ratio for the (103) peak increased to 0.2 (Fig. 6b), which was consistent with the high degree of misalignment observed in SEM (Fig. 5c). On polycrystalline ITO substrates, which have rms roughness values of 0.67 nm to 1.22 nm depending on the ITO thickness, we were able to grow highly aligned ZnO NRAs similar to the results on Si. This suggests that the difference in substrate orientation between polycrystalline FTO and single crystal Si(100) does not strongly affect the ZnO NRA alignment. Instead, substrate roughness plays an important role in determining the morphology of the ZnO NRA. To achieve highly aligned, dense ZnO nanorods, the substrate roughness should be lower than or equal to the seed layer roughness (~ 2 nm).

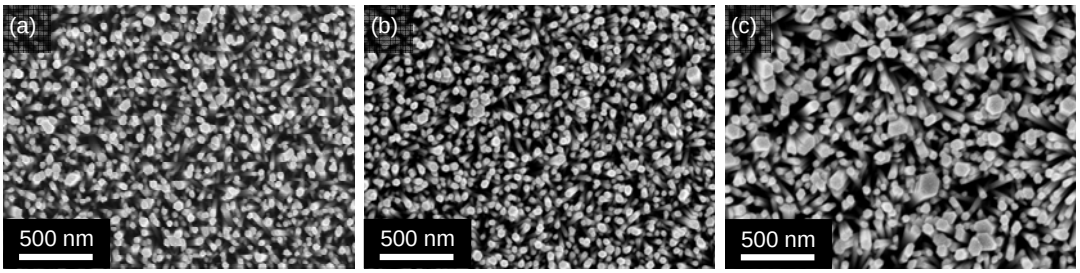

Fig. 5. Plane view SEM of ZnO NRAs grown on FTO-coated glass substrates with rms roughness (sheet resistance) values of (a) 8.14 nm (1000 Ω/sq), (b) 15.77 nm (15 Ω/sq), and (c) 48.71 nm (7 Ω/sq).

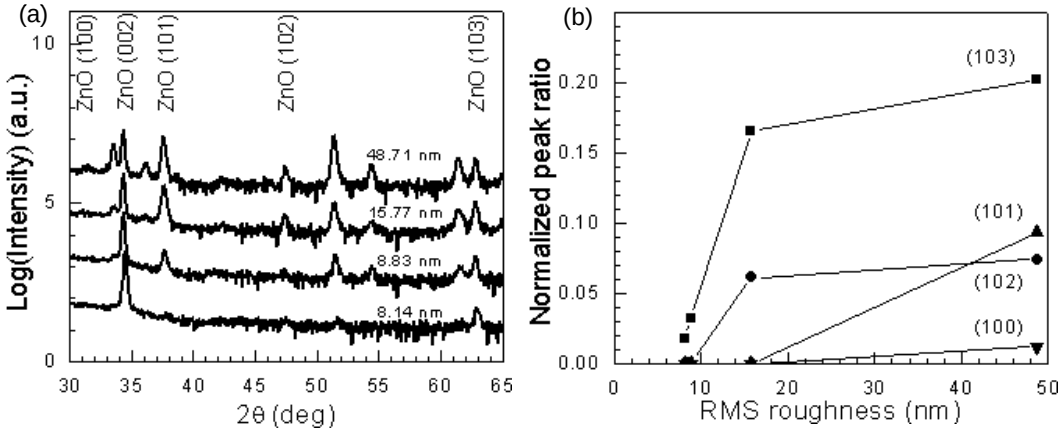

Fig. 6. (a) XRD spectra of ZnO NRAs grown on FTO-coated substrates with different rms roughness values (from top to bottom: 48.71 nm, 15.77 nm, 8.83 nm, 8.14 nm). The plots are offset for clarity. (b) Normalized ZnO peak ratios for (103) (squares), (102) (circles), (101) (triangles), and (100) (inverted triangles) as a function of substrate roughness.

Conclusions

We demonstrated that the alignment, density, diameter, and length of ZnO NRAs fabricated using a two-step method are strongly influenced by the relative humidity during the seeding step and the roughness of the underlying substrate. From SEM, XRD, and PL data, we determined that a minimum RH of ~ 20% was required to grow highly aligned, close-packed ZnO NRAs on smooth substrates. An optimal RH of ~ 35% resulted in the greatest uniformity in nanorod diameter and length. From AFM and contact angle results, we concluded that the ambient water vapor is required in the formation of ZnO seeds. Finally, SEM and XRD data indicate that the degree of alignment of ZnO NRAs strongly depended on the substrate roughness. With an improved understanding of the relationship between processing conditions and resulting structure of the ZnO NRAs, we are working towards optimization of the NRAs as electron acceptors for organic-inorganic PV devices.

References

S. E. Shaheen, D. S. Ginley, G. E. Jabbour, MRS Bull. 30 (2005) 10.

F. Padinger, R. S. Rittberger, N. S. Sariciftci, Adv. Func. Mater. 13 (2003) 85.

G. Li, V. Shrotriya, J. Huang, Y. Yao, T. Moriarty, K. Emery, Y. Yang, Nat. Mat. 4 (2005) 864.

W. U. Huyng, J. J. Dittmer, A. P. Alivisatos, Science 295 (2002) 2425.

W. J. E. Beek, M. M. Wienk, R. A. J. Janssen, Adv. Mater. 15 (2003),1009.

K. M. Coakley, Y. Liu, M. D. McGehee, K. L. Frindell, G. D. Stucky, Adv. Func. Mater. 13 (2003) 301.

P. A. van Hal, M. M. Wienk, J. M. Kroon, W. J. H. Verhees, L. H. Sloof, W. J. H. van Gennip, P. Jonkheijm, R. A. J. Janssen, Adv. Mater. 15 (2003) 118.

R. Konenkamp, L. Dloczik, K. Ernst, C. Olecsh, Physica E. 14 (2002) 219.

L. Vayssieres, K. Keis, S.-E. Lindquist, A. Hagfeldt, J. Phys. Chem. B. 105 (2001) 3350.

Z. R. Tian, J. A. Voigt, J. Liu, B. McKenzie, M. J. McDermott, M. A. Rodriguez, H. Konishi, H. Xu, Nat. Mat. 2 (2003) 821.

L. E. Greene, M. Law, J. Goldberger, F. Kim, J. C. Johnson, Y. Zhang, R. J. Saykally, P. Yang, Angew. Chem. Int. Ed. 42 (2003) 3031.

L. E. Greene, M. Law, D. H. Tan, M. Montano, J. Goldberger, G. Somorjai, P. Yang, Nano. Lett. 5 (2005) 1231.

J. W. P. Hsu, D. R. Tallant, R. L. Simpson, N. A. Missert, R. G. Copeland, Appl. Phys. Lett. 88 (2006) 252103.

M. Law, L. E. Greene, J. C. Johnson, R. Saykally, P. Yang, Nat. Mat. 4 (2005) 455.

D. C. Olson, J. Piris, R. T. Collins, S. E. Shaheen, D. S. Ginley, Thin Solid Films 496 (2006) 26.

Y. Kim, S. Cook, S. M. Tuladhar, S. A. Choulis, J. Nelson, J. R. Durrant, D. D. C. Bradley, M. Giles, I. McCulloch, C.-S. Ha, M. Ree, Nat. Mater. 5 (2006) 197.

Tunable Arrays of ZnO Nanorods and Nanoneedles via Seed Layer and Solution Chemistry

Introduction

ZnO nanorod arrays with tunable alignment and morphology have attracted much recent attention due to the potential for producing optimized nanostructures for energy conversion, catalysis, sensing, and other applications. ZnO exhibits a combination of interesting properties including wide band gap (E_g = 3.3 eV), high exciton binding energy (60 meV),[1] high electron mobility (100 $cm^2 V^{-1} s^{-1}$),[2] and piezoelectricity,[3,4] with many potential applications in electronic and optoelectronic devices.[1,5,6] By controlling the reaction conditions during heterogeneous deposition of ZnO from aqueous solutions, tunable nanostructures can be readily fabricated.[7-22] Many researchers have utilized growth solutions with different pHs to deposit ZnO nanorod arrays (NRAs) and nanoneedle arrays (NNAs) with distinct morphologies.[7-17] For example, near neutral growth solutions containing the weak base hexamethylene tetraamine (HMT) generally resulted in nanorods with well-defined {10$\underline{1}$0} facets on both planar[7-11] and patterned[12-14] substrates. Growth solutions containing ammonia with pH from 10 to 10.5 were found to deposit ZnO NNAs with different degrees of alignment.[15,16] Highly basic growth solutions (pH 13 to 14) containing NaOH yielded nanorods with circular cross sections, i.e. poorly defined {10$\underline{1}$0} facets.[17] Despite these reports, a systematic study of the effect of solution pH on the growth dynamics and morphologies of ZnO NRAs has not been reported.

In order to control the alignment and morphologies of ZnO NRAs and NNAs, we and other groups have also utilized different seed layers for ZnO deposition.[8,9,11,20] Piezoelectric force microscopy has shown that the ZnO nanorods grow in the [0001] direction in solution.[19] Hence, by controlling the crystallographic orientation of a lattice matched seed layer, e.g. ZnO, we can control the alignment of ZnO nanorods. For example, using substrates coated with a submonolayer of ZnO nanoparticles as the seed layers, NRAs with low degree of alignment were fabricated due to the random direction of the <0001> growth axis on the nanoparticle seeds.[8,20] In contrast, using highly oriented ZnO films with <0001> direction perpendicular to the substrate as the seed layers, we and others have demonstrated the growth of vertically aligned ZnO NRAs.[9,11] We have also demonstrated more complex ZnO nanostructures such as higher order branched NNAs using a sequential nucleation and growth process in solutions containing organic molecules such as citric acid and diamines.[20-22] However, a systematic comparison of the ZnO nanostructures grown on different seed layers has not yet been performed. In this report, we present a quantitative analysis on the effects of growth solution pH and the growth modifier 1,3-diaminopropane (DAP) concentration on the crystal growth rate and the resulting morphology of ZnO NRAs and NNAs grown on different seed layers.

Experimental Procedure

Zinc acetate dihydrate (99.999%, Aldrich), zinc nitrate hexahydrate (Fisher), NaOH (Fisher), DAP (Aldrich), and HMT (Fisher) were used as received. To study the effect of growth solution pH on NRA morphology, we first deposited oriented ZnO films on Si substrates by coating them multiple times with an 5 mM ethanolic solution of zinc acetate dihydrate at a relative humidity of

~ 35%, followed by conversion to ZnO in a 350 °C furnace.[9,11] We then placed the substrates in solutions with either 25 mM $Zn(NO_3)_2$ and HMT at 92.5 °C ("HMT recipe")[9-11] or 1 mM $Zn(NO_3)_2$ and 90 mM NaOH at 70 °C with stirring ("NaOH recipe")[17] for various amounts of time to grow the ZnO NRAs. To study the effect of DAP concentration ([DAP]) on ZnO NNA morphology, two other types of seed layers were prepared in addition to the oriented ZnO film. For a seed layer of nanoparticles, a cleaned glass slide was briefly dipped in an aqueous suspension of ZnO nanoparticles and allowed to dry.[20] For a seed layer of ZnO microrods with ~ 1 μm diameter, a cleaned glass slide was first placed in aqueous solution of 20 mM $Zn(NO_3)_2$ and HMT at 60 °C for overnight.[21] After each substrate had been seeded, it was then incubated in an aqueous solution of 20 mM $Zn(NO_3)_2$, 20 mM HMT, and 40 mM to 190 mM DAP at 60 °C for 18 hours to grow the NNAs. The dimensions and morphology of the ZnO NRAs and NNAs were characterized by a Zeiss field-emission source scanning electron microscope (SEM). Crystallinity and degree of alignment were determined by x-ray diffractometry (XRD, Rigaku) with Cu Kα radiation. The average nanorod diameter was also approximated by the crystalline domain size calculated from ZnO (0002) peak using the Scherer equation $t = 0.9 \lambda / (B \cos \theta)$, where t is the domain size, λ is the x-ray wavelength, and B is the angular FWHM of the peak at angle θ. Speciation diagrams were produced using Geochemist's Workbench (GWB Software, Golden, CO), which generates species distribution and stability diagrams versus activity based on the Minteq database of thermodynamic data.

Results and Discussion

Effect of Solution pH

We found that different growth solution pH significantly altered the growth rate and morphology of ZnO NRAs on highly oriented ZnO seed layers. As shown by the zinc speciation diagrams for activities of 25 mM (Fig. 1a) and 1 mM (Fig. 1b), the growth solution is saturated at room temperature with Zn^{2+} for HMT recipe and $Zn(OH)_4^{2-}$ for NaOH recipe respectively. As the solution is heated to the reaction temperature, denoted by a cross in Figure 1, the zincite (ZnO) phase becomes thermodynamically favored, and the zinc ions reacts on the seed layer via hydrolysis and condensation to initiate nanorod growth. We should note that the HMT growth solution has a pH of ~ 6.8, while the same solution without HMT has a pH of ~ 5.5. Thus, by maintaining solution pH, HMT helps regulate the growth of ZnO. Despite using the same type of seed layer, significant differences in ZnO NRA morphology were observed between neutral and high pH growth solutions. For example, for NRAs of approximately equal length (500 nm), the NaOH recipe (Fig. 2b) resulted in NRAs with average nanorod diameters of ~ 35 nm compared to ~ 50 nm for the HMT recipe (Fig. 2a). XRD data indicate that both ZnO NRAs are highly aligned with only ZnO (0002) peak present (Fig. 2c). From the width of the peak, we determined the average minimum crystalline domain size, which also corresponds to the average nanorod diameter since each nanorod is a single crystal.[9] For NRAs of 500 nm length, we found a nanorod diameter of 47 nm and 34 nm grown using the HMT and the NaOH method, respectively, in good agreement with SEM data. Due to the smaller diameters, NRAs using the NaOH recipe occupied a smaller volume fraction than those grown by the HMT recipe, as evident in Figure 2b by the greater amount of space between the nanorods. The smaller volume fraction is consistent with the ratio of integrated XRD intensity for the ZnO (0002) peak for NaOH versus HMT recipe, which is ~ 0.6 (Fig. 2c). The HMT recipe also yielded nanorods with well defined {10$\underline{1}$0} facets and hexagonal cross sections as shown in the plane view SEM image

(Fig. 2a). In contrast, the NaOH recipe results in nanorods that are much less faceted, with a rounded cross section (Fig. 2b).

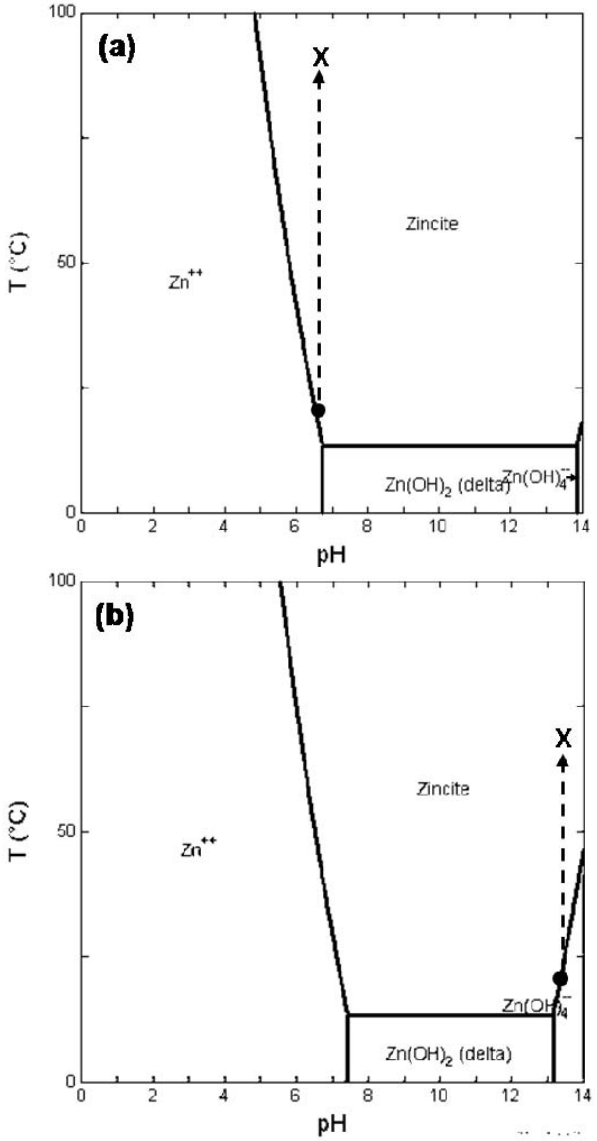

Figure 1: Speciation diagram of Zn as a function of pH and temperature in aqueous solutions containing Zn activity of a) 25 mM (HMT recipe) and b) 1 mM (NaOH recipe). The initial temperature is marked by the circle and the growth temperature is marked by the cross.

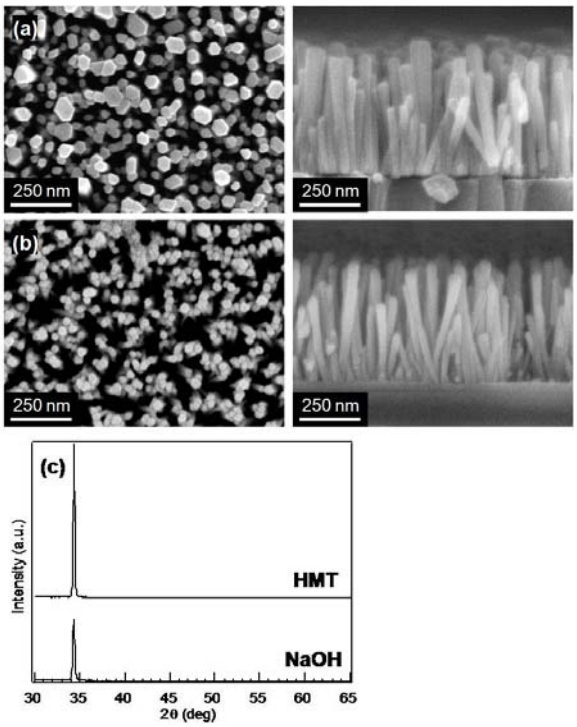

Figure 2: Comparison of ZnO NRAs of ~ 500 nm length grown in different pH solutions. a) Plane view (left) and cross sectional (right) SEM of NRA via HMT recipe (pH ~ 6.8), growth time = 115 min. b) Plane view (left) and cross sectional (right) SEM of NRA via NaOH recipe (pH ~ 13.2), growth time = 70 min. c) XRD data of the NRAs via HMT (top) and NaOH (bottom) recipes.

Comparison of ZnO NRAs dimensions as a function of growth time using HMT and NaOH recipes reveals additional information on ZnO nanorod growth dynamics. First, nanorod length linearly increased at a fitted rate of 8.2 nm / min for the NaOH recipe compared to 4.4 nm / min for the HMT recipe (Fig. 3a), confirming that high pH causes an increase in the absolute deposition rate on the ZnO (0001) surface. While nanorod diameter for the NaOH recipe is consistently smaller than that for the HMT recipe, the growth rate of nanorod diameter is similar for both recipes (Fig. 3b, triangles). We also found that a linear fit of nanorod diameter versus growth time yielded positive intercepts for time = 0 (Fig. 3b, triangles), which is also the case even if we take into account the time needed to the solution to reach the growth temperature (~ 20 min). This suggests that nanorod diameter increased rapidly during initial stages of growth for both recipes, in contrast to the linear growth in nanorod length. Plotting nanorod aspect ratio as a function of growth time, we again found a faster linear increase of 0.23 / min for the NaOH recipe versus 0.096 / min for the HMT recipe (Fig. 3b, circles), indicating that deposition on the (0001) surface is preferentially enhanced over the {10$\underline{1}$0} surfaces. These results can be explained by the different charge on the zinc ions for HMT and NaOH recipe, which are Zn^{2+} and $Zn(OH)_4^{2-}$, respectively (Fig. 1). Because the ZnO (0001) surface is positively charged,[23] the negatively charged $Zn(OH)_4^{2-}$ may be preferentially attracted to the growth facet. In contrast, since the {10$\underline{1}$0} surfaces are uncharged, no significant difference in the diameter growth rate is expected. In short, high solution pH preferentially enhanced growth of ZnO NRAs along the <0001> direction both in absolute magnitude and also in comparison to other crystallographic directions, possibly due to attractive interactions between $Zn(OH)_4^{2-}$ ions and the positively

charged Zn terminated (0001) surface. As a result, a shorter growth time is required for the deposition of ZnO NRAs of a given length using the NaOH recipe, leading to smaller nanorod diameter, poor faceting, and lower NRA volume fraction.

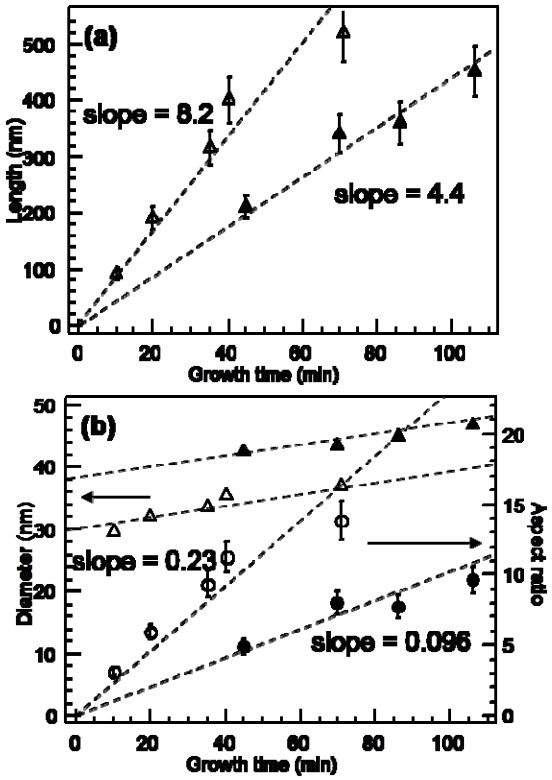

Figure 3: Dimensions of nanorods deposited on oriented ZnO using the HMT (closed symbols) and NaOH (open symbols) recipe. a) Nanorod length from SEM versus growth time. Linear fit to length data (dashed) and growth rate (slope of linear fit) are also shown. b) Diameter from XRD (triangles) and aspect ratio (circles) versus growth time. Linear fit to aspect ratio data (dashed) and slope are also shown. Dashed lines for diameter are guides to the eyes only because of non-zero intercept.

Effect of DAP Concentration

DAP mediates the growth of ZnO nanoneedles in a qualitatively similar fashion on the three seed layers that we examined. However, the concentration range at which the mediation occurs and the morphology and alignment of the deposited nanoneedles differ between seed layer types. It should be noted that since DAP is a base, the growth solution pH increased with the addition of DAP, from ~ 10 at [DAP] = 43 mM to ~ 12 at [DAP] = 190 mM. Although the speciation diagrams in Fig. 1 suggest that zinc is normally not soluble over these pH ranges at room temperature, we found the growth solution to be transparent for [DAP] > 43 mM due to the formation of soluble zinc-amino complex.[21,22] When we compared ZnO deposition in the presence of DAP on three seed layers, we noticed two major effects. First, in contrast to the NaOH recipe where only the pH was adjusted, solutions containing DAP resulted in nanorods with tapered tips, or nanoneedles, and the extent of the tapered region became longer at higher [DAP] (Figs. 4a and 4b). We previously proposed that the tapering may be caused by reversible

adsorption of DAP to the (0001) facet of ZnO during growth, which retards Ostwald ripening and preserves minute (0001) steps to create the tapered tip profile.[21]

Second, the seed layer strongly influenced ZnO volume fraction and alignment of the NNAs. For example, an oriented ZnO seed layer yielded close packed, highly aligned ZnO NNAs at all [DAP] (Fig. 4a). The densely packed seed layer with the (0001) growth facet oriented parallel to the substrate[9] allowed for unimpeded growth of the nanoneedles, thus maximizing alignment and NNA volume fraction. In contrast, a nanoparticle seed layer led to less aligned ZnO NNAs with decreasing volume fraction at increasing [DAP] (Fig. 4b). Due to the random orientation of the (0001) facet on the nanoparticles with respect to the substrate, the ZnO nanoneedles grew in random directions, causing many to impinge on the substrate or other nanoneedles, which terminated growth and decreased NNA volume fraction. On a seed layer of ZnO microrods, the nanoneedles grew primarily on the {10$\underline{1}$0} facets of the microrods, and the nanoneedle c-axis were oriented at ~ 80° to the microrod c-axis for all [DAP] due to an energetically favored twin configuration.[21] The packing density of the ZnO branch arrays was independent of [DAP] up to [DAP] ~ 125 mM (Fig. 4c), at which point the volume fraction diminished sharply with [DAP]. Previously we showed that DAP caused the nucleation of a layer of polycrystalline ZnO on the microrod to act as the seed layer, but for [DAP] > 125 mM, the level of zinc supersaturation was too low to overcome the free energy of nucleation of seeds on the {10$\underline{1}$0} surfaces, so no nuclei were formed. [21,22] Thus, at [DAP] = 125 mM, nucleation was slow and sparse on the microrod surface, and for [DAP] > 125 mM no needle growth was observed.

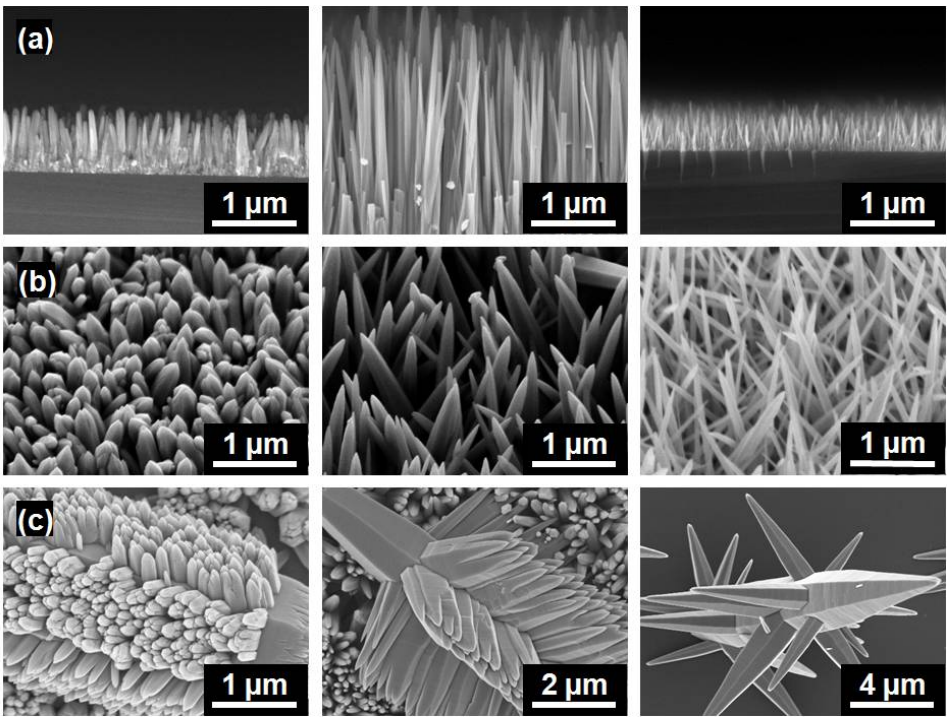

Figure 4: Comparison of ZnO nanoneedle arrays grown at different [DAP] on three seed layers. a) Cross sectional view on oriented ZnO film; from left, 40 mM, 125 mM, 190 mM. b) 40° tilt view on ZnO nanoparticles; from left, 40 mM, 125 mM, 190 mM. c) Plane view on ZnO microrods; from left, 40 mM, 80 mM, 125 mM. No branch growth was observed at [DAP] > 125 mM.

When the characteristic dimensions of the nanoneedle arrays for the three types of substrates were extracted from SEM images, their dependence on [DAP] and seed layer type became apparent. On oriented ZnO film and ZnO microrod seed layers, the average nanoneedle length increased with [DAP] at different rates and reached maximum values of 3.65 μm and 8.9 μm respectively at [DAP] = 125 mM after 18 hours (Fig. 5a). In addition, a ZnO NNA on microrods exhibited a consistently larger length compared to a NNA on oriented ZnO film at the same [DAP]. For [DAP] > 125 mM, the average nanoneedle length decreased on oriented ZnO films, and no ZnO nanoneedles were observed on ZnO microrods due to a lack of nucleation sites, as previously mentioned. In contrast, the average nanoneedle length on ZnO nanoparticles continued to increase as [DAP] increased above 125 mM (Fig. 4b), although we could not quantitatively measure the length due to the random alignment of the nanoneedles. The average nanoneedle diameter on all three seed layer types increased as a function of [DAP] until maximum values were reached at [DAP] = 80 mM to 125 mM. At higher [DAP], the average nanoneedle diameter decreased for NNAs on oriented ZnO films (Fig. 5b, squares) and ZnO nanoparticles (Fig. 5b, circles), and became zero on ZnO microrods as new ZnO crystals did not nucleate. For a ZnO NNA on oriented ZnO film at [DAP] = 190 mM, we found an average nanoneedle diameter of 17 nm, which is the smallest value that we know of using non-hydrothermal aqueous growth. Comparing the average nanoneedle diameter for the three seed layers at the same [DAP], we again found that an oriented ZnO film generally yielded the smallest diameter, followed by nanoparticles and then by microrods. Finally, NNAs on microrods exhibited a constant aspect ratio of ~ 4.5 for all [DAP] (Fig. 5c, triangles), whereas NNAs on oriented ZnO films exhibited various aspect ratios with a maximum value of ~ 50 at [DAP] = 125 mM (Fig. 5c, squares).

The trend in nanoneedle dimensions versus [DAP] may be explained by the following combination of factors. First, chelation by DAP decreases supersaturation of zinc ions, which tends to decrease the growth rate of ZnO nanoneedles. However, it also enhances heterogeneous versus homogeneous growth, as seen by the fact that growth solutions with [DAP] $\geq$ 80 mM contained no ZnO precipitate which nucleated homogeneously from solution. As a result, ZnO may be preferentially deposited on the nanoneedles at [DAP] $\leq$ 125 mM, leading to increased growth rate for both length and diameter. In contrast, at [DAP] > 125 mM, the additional chelation may decrease supersaturation sufficiently to hinder the growth of ZnO nanoneedles.

Second, due to differences in orientation and surface coverage between seed layers, the areal density of viable nuclei, i. e. those which led to full length nanoneedles, was highest for oriented ZnO film, followed by nanoparticles and finally the sparsely coated ZnO microrods. Since the zinc content was constant for all growth solution and the growth time of 18 hr was sufficiently long to carry the reaction to completion,[22] it is reasonable the dimensions per nanoneedle were generally smallest on oriented ZnO film (Figs. 5a and 5b, squares) and largest on ZnO microrods (Figs. 5a and 5b, triangles). In addition, the lower viable nuclei density on ZnO nanoparticles compared to oriented ZnO film may decrease the amount of ZnO deposited from solution per unit time so that the ZnO nanoneedles grow in the [0001] direction for a longer period of time before the zinc concentration falls below the supersaturation limit. This may explain the continued increase in nanoneedle length versus [DAP] on nanoparticle seed layers (Fig. 4b). Finally, ZnO nanoneedles on microrods were shown to coalesce during growth into larger

nanoneedles in the presence of DAP,[22] which further explains their larger dimensions (Figs. 5a and 5b, triangles) and increased spacing between nanoneedles (Fig. 4c) as [DAP] increases. Coalescence does not appear to occur for ZnO NNAs deposited on oriented ZnO film and on ZnO nanoparticles, possibly because each nanoneedle grows from a discrete nanocrystal, which is not perfectly aligned with the other nanocrystal seeds.

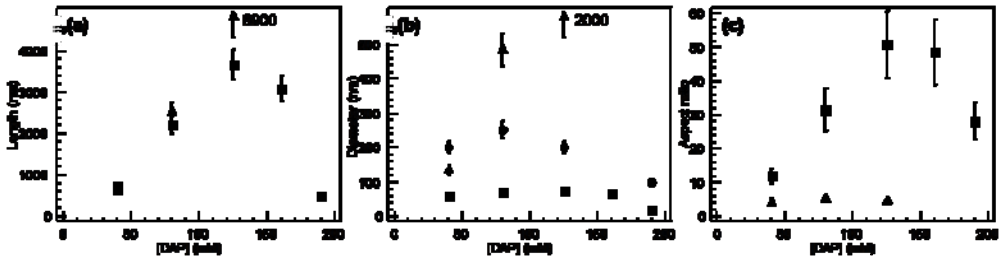

Figure 5: Dimensions of NNAs deposited on oriented ZnO film (squares), ZnO microrods (triangles), and ZnO nanoparticles (circles) under identical growth conditions for 18 hours as a function of DAP concentration. a) Length. b) Diameter. c) Aspect ratio. Average nanoneedle length and aspect ratio were not determined for NNAs on nanoparticles due to low degree of orientation.

Conclusions

We demonstrated that the dimensions and morphology of ZnO nanorods arrays and nanoneedle arrays can be controlled by varying growth solution pH and DAP concentration on different types of seed layers. Increasing the growth solution pH from near neutral to highly basic conditions using NaOH resulted in increased deposition on the (0001) surface and reduced deposition on and faceting of the {10$\underline{1}$0} surfaces, possibly due to favorable interactions between $Zn(OH)_4^{2-}$ ions at high pH and the positively charged (0001) surface. Increasing the DAP concentration from 43 mM to 190 mM created NNAs with more pronounced tip tapering, while nanoneedle length and diameter reached their maximum values at [DAP] ~ 125 mM. Further increases in DAP concentration decreased the nanoneedle diameter while varying the nanoneedle length in a complex fashion depending on the seed layer. The aspect ratio of NNAs on oriented ZnO film reached a maximum of ~ 50 at [DAP] = 125 mM, whereas the aspect ratio on ZnO microrods remained constant at ~ 4.5. We explain the trends in nanoneedle dimensions, alignment, and volume fraction via a combination of zinc chelation by DAP, interplay between the finite zinc supply in solution and the number density ZnO nanoneedles on different seed layers, and details in nucleation and coalescence of ZnO nanoneedles on microrod seed layers. With an improved understanding of the relationship between growth conditions and resulting morphology of the ZnO nanostructures, we will be able to optimize ZnO nanostructures for specific applications.

References

Huang, M. H.; Mao, S.; Feick, H; Yan, H.; Wu, Y.; Kind, H.; Weber, E.; Russo, R.; Yang, P. *Science* **2001**, *292*, 1897.

Konenkamp, R.; Dloczik, L.; Ernst, K.; Olecsh, C. *Physica E* **2002**, *14*, 219.

Yamamoto, T.; Shiosaki, T.; Kawabata, A. *J. Appl. Phys.* **1980**, *51*, 3113.

Wang, Z. L.; Song, J. *Science* **2006**, *312*, 242.

Look, D. C. *Mater. Sci. Eng. B* **2001**, 80, 383.

Yang, P.; Yan, H. Q.; Mao, S.; Russo, R.; Johnson, J.; Saykally, R.; Morris, N.; Pham, J.; He, R. R.; Choi, H. J. *Adv. Funct. Mater.* **2002**, *12*, 323.

Vayssieres, L.; Keis, K.; Lindquist, S.-E.; Hagfeldt, A. *J. Phys. Chem. B.* **2001**, *105*, 3350.

Greene, L. E.; Law, M.; Goldberger, J.; Kim, F.; Johnson, J. C.; Zhang, Y.; Saykally, R. J.; Yang, P. *Angew. Chem. Int. Ed.* **2003**, *42*, 3031.

L. E. Greene, M. Law, D. H. Tan, M. Montano, J. Goldberger, G. Somorjai, P. Yang, *Nano. Lett.* **2005**, *5*, 1231.

K. Govender, D. S. Boyle, P. B. Kenway, P. O'Brien *J. Mater. Chem.* **2004**, *14*, 2575.

Lee, Y.-J.; Sounart, T. L.; Scrymgeour, D. A.; Voigt, J. A.; Hsu, J. W. *J. Cryst. Gro.* **2007**, *304*, 80.

Hsu, J. W. P.; Tian, Z. R.; Simmons, N. C.; Matzke, C. M.; Voigt, J. A.; Liu, J. *Nano Lett.* **2005**, *5*, 83.

Hsiao, C.-S.; Peng, C.-H.; Chen, S.-Y. *J. Vac. Sci. Technol. B* **2006**, *24*, 288.

Gui, Z.; Wang, X.; Liu, J.; Yan, S.; Ding, Y.; Wang, Z.; Hu, Y.; *J. Sol. Stat. Chem.* **2006**, *179*, 1984.

Tak, Y.; Yong, K. *J. Phys. Chem. B* **2005**, *109*, 19263.

Xu, F.; Yuan, Z.-Y.; Du, G.-H.; Ren, T.-Z.; Bouvy, C.; Halasa, M.; Su, B.-L. *Nanotech.* **2006**, *17*, 588.

Peterson, R. B.; Fields, C. L.; Gregg, B. A. *Langmuir* **2004**, *20*, 5114.

Cui, J.; Gibson, U. J. *J. Phys. Chem. B* **2005**, *109*, 2207.

Scrymgeour, D. A. ; Sounart, T. L.; Simmons, N. C.; Hsu, J. W. P. *J. Appl. Phys.* **2007**, *101*, 014316.

Tian, Z. R.; Voigt, J. A.; Liu, J.; McKenzie, B. B.; McDermott, M. J.; Rodriguez, M. A.; Konishi, H.; Xu, H. *Nat. Mat.* **2003**, *2*, 821.

Sounart, T. L.; Liu, J.; Voigt, J. A.; Hsu, J. W. P.; Spoerke, E. D.; Tian, Z. R.; Jiang, Y. *Adv. Func. Mat.* **2006**, *16*, 335.

Sounart, T. L.; Liu, J.; Voigt, J. A.; Huo, M.; Spoerke, E. D.; McKenzie, B. B. *J. Am. Chem. Soc.*, in press, published on the web 11/29/07.

Gao, P. X.; Wang, Z. L. *J. Appl. Phys.* **2005**, *97*, 044304.

ZnO Nanostructures as Efficient Antireflection Layers in Solar Cells

Introduction

Antireflection coatings (ARCs) play a major role in enhancing the efficiency of photovoltaic (PV) devices by increasing light coupling into the active region of the devices. On lithographically patterned Si PV devices, various groups have fabricated surface textured ARCs by anisotropic etching,[1] etching through patterned masks,[2-5] or via other techniques that generate porosity and/or roughness.[6-8] The textured surface traps light, leading to a broadband suppression in reflection. For thin film PV devices (e.g. amorphous Si, CdTe, $CdInGaSe_2$), ARCs generally consist of one or more dielectric layer(s), either in the form of a quarter wave thickness film that exhibits a wavelength sensitive reduction in reflection due to interference,[9-15] or as a nanoporous film that takes advantage of light trapping for a more broadband response.[16,17] Recently, Xi et al. utilized oblique-angle deposition at different angles to create 5 layers of TiO_2 and SiO_2 nanorods with an optimized overall refractive index gradient, and achieved an extremely low reflectance.[18] In their case, discontinuous refraction index changes between layers with different volume fractions of dielectrics created the desired refractive index profile. In this letter, we report the effects of highly textured ZnO nanorod arrays (NRAs), synthesized via low temperature solution growth, on ARC performance. By changing the growth conditions, we modify the shape of the ZnO nanorod tips, leading to continuously varying refractive index profiles in a single layer. Subtle changes in the nanorod tip shape result in significantly improved antireflection properties, in good agreement with predictions from rigorous coupled wave analysis (RCWA). Because our approach is substrate independent, these textured ZnO ARCs may be applicable to a wide variety of PV devices and other antireflection applications.

Experimental Results

ZnO is attractive as a dielectric ARC material because of its good transparency, appropriate refractive index ($n = 2$), and ability to form textured coating via anisotropic growth. For example, textured ZnO films deposited on Si via MOCVD demonstrated superior ARC performance compared to a TiO_2 single layer ARC (SLARC).[12] We synthesized ZnO NRA ARCs using a two-step seeding and growth method on *n*-type Si(100) (Allied Bendix).[19,20] The seeding process was carried out at room temperature at 35% relative humidity, the optimal condition for producing ordered NRAs.[20] Seeded substrates were placed in aqueous solutions containing zinc nitrate (Fisher) and hexamethylene tetraamine (HMT, Fisher) at 92.5 °C or 60 °C. Several concentrations of 1,3-diaminopropane (DAP, Acros) was also added to control the tapering of nanorods; see Supporting Information for the full list of ZnO NRAs and their synthesis conditions.[21,22] An example of a ZnO NRA in cross section imaged with a scanning electron microscope (SEM) is shown in Fig. 1a. For comparison, a 0.55 μm thick porous ZnO film was also deposited on Si via multiple steps of spin coating a sol of 2 M zinc acetate (Aldrich) and 2 M ethanolamine (Aldrich) in 2-methoxyethanol (Aldrich) at 2000 rpm followed by heating on a hot plate at 300 °C for 5 min.[23]

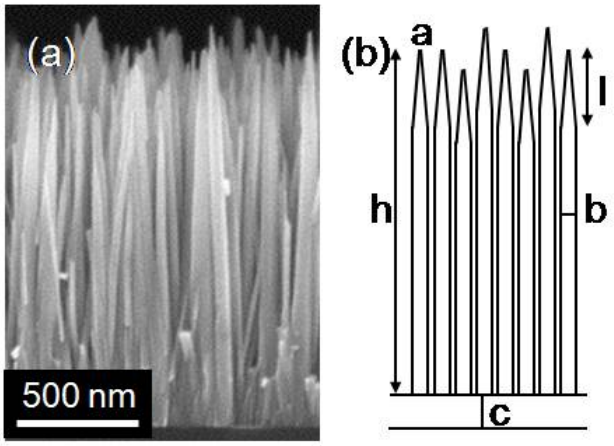

Figure 1: Example of a ZnO NRA. a) Cross section SEM image of a highly tapered ZnO NRA (190 mM DAP, 60 °C growth temperature, 18 h growth time). b) schematic representation of the corresponding nanorod parameters extracted via software analysis.

ARC structure was characterized by field emission SEM (Zeiss) and x-ray diffraction (XRD, Rigaku). Analyzing cross sectional SEM images of each ZnO NRA (e.g. Fig. 1a) using ImageJ, we obtained average value over at least five measurements for various parameters including nanorod tip diameter *a*, diameter of the non-tapered region *b*, thickness of the fused base layer *c*, overall nanorod length *h*, and length of the tapered region *l*, as schematically represented in Fig. 1b. From the top view SEM images, we also determined via software analysis the area fraction of ZnO (~ 0.7 for all NRAs) and used it as the NRA volume fraction *f* of the non-tapered region, because nanorods synthesized using the two step seeding and growth procedure are vertically oriented.[19,20] Absolute hemispherical reflectance measurements were carried out with a UV-vis-near IR spectrophotometer (Cary) and an integrating sphere (Labsphere) with a sampling spot of 3 mm x 13 mm at normal incidence. Weighted reflectance R_w was calculated by normalizing the reflectance spectra with the internal quantum efficiency spectra of a typical multicrystalline Si solar cell and the terrestrial global solar spectrum (AM1.5).[9] Comparisons with a multicrystalline Si solar cell with a silicon nitride (SiN) SLARC were made.

Variations in the NRA growth conditions strongly influenced the morphology of the textured ZnO ARCs, as shown by the SEM images (Fig. 2). For example, at a growth temperature of 92.5 °C, the tips of the ZnO nanorods changed from a flat top (Fig. 2a) to a tapered shape (Fig. 2c) with the addition of DAP in the growth solution. In the presence of DAP, an increase in growth time simultaneously increased nanorod length and decreased tip diameter, as seen for samples grown for 30 min (Fig. 2b) and 45 min (Fig. 2c). Decreasing the growth temperature to 60 °C significantly reduced the growth rate, while creating highly tapered nanorods with tip diameter of ~ 10 nm (Fig. 2d). XRD spectra of all ZnO NRAs revealed a strong (002) peak at $2\theta = 34.4°$ (Fig. 2f) and no other crystallographic peaks, indicating that the nanorods are highly aligned, in agreement with SEM images. In contrast, the sol-gel ZnO film contained unaligned pores (Fig. 2e) and randomly oriented crystallites (Fig. 2f).

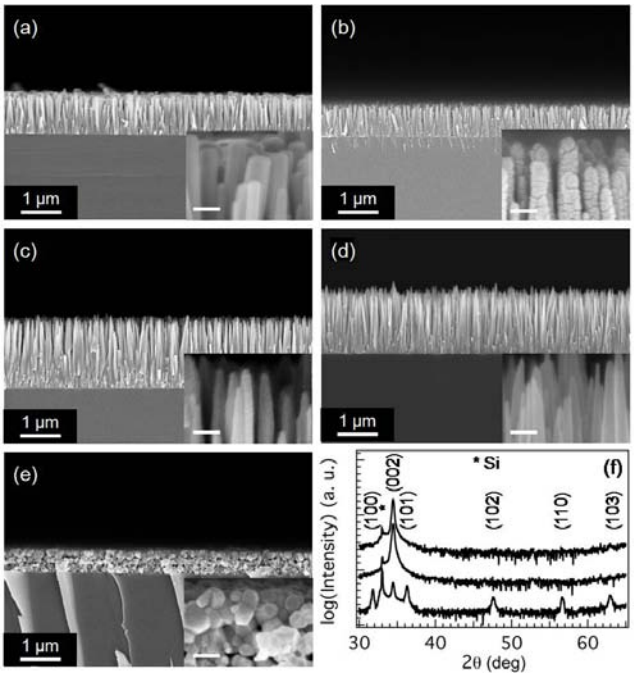

Figure 2: Cross section SEM images of nanostructured ZnO ARCs deposited under different conditions. a) flat top nanorods. b) tapered nanorods, 30 min growth time. c) tapered nanorods, 45 min growth time. d) Highly tapered nanorods, 18 h growth time. e) Sol-gel film. Inset, high magnification view of the samples (scale bar, 100 nm). f) XRD spectra of flat top nanorods (top), highly tapered nanorods (middle), and sol-gel film (bottom), with ZnO peaks indexed.

Comparisons of the reflectance spectra of ZnO NRAs with each other and with other dielectric films reveal the importance of morphology on ARC performance. First, all NRAs exhibited significantly lower reflectance spectra (Fig. 3) and R_w values (Table 1) compared to the sol-gel ZnO film with randomly oriented ~ 200 nm diameter pores. In other words, a combination of increased pore alignment and decreased pore diameter appears to improve antireflection response. Second, compared to a ZnO NRA with a flat top surface (Fig. 3, red), a tapered NRA synthesized in the presence of DAP eliminated the optical interference fringes (Fig. 3, orange). The elimination of interference is due to a rough ZnO-air interface from tapering of the nanorod tips (Fig. 2c, inset) and variation in nanorod length, as will be shown later. More significantly, differences in NRA morphology caused by changing the synthesis conditions significantly altered the macroscale ARC response. For example, the tapered NRA grown at 92.5 °C exhibited a weak monotonic decrease in reflectance with wavelength (Fig. 3, orange), resulting in a relatively high R_w of 13.6% (Table 1). The highly tapered NRA grown at 60 °C showed the same trend but with a stronger wavelength dependence and significantly lower reflectance for wavelengths greater than 500 nm (Fig. 3, black), leading to R_w of 6.6% (Table 1). In contrast, an optimized quarter wavelength SiN SLARC on a multicrystalline-Si solar cell exhibited highly wavelength dependent reflectance response (Fig. 3, blue) with a minimum at 640 nm due to destructive interference, and a R_w of 7.8% after subtracting the contribution from metallic contacts.[9] While the highly tapered NRA did not reach the same minimum visible reflectance compared to the SLARC, its significantly reduced wavelength dependence and the enhanced reflectance suppression between 700 nm and 1200 nm are primarily responsible for the improvement in R_w. In short, orientation of the air pores, roughening of the ZnO-air interface,

and morphological changes such as nanorod tip tapering all contribute to the improvement in the performance of ZnO NRA ARCs.

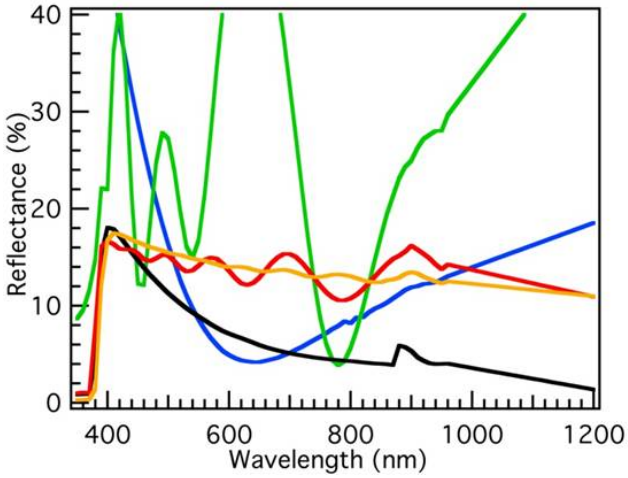

Figure 3: Front reflectance spectra of flat top NRA (red), tapered NRA (orange), sol-gel film (green), optimized SiN SLARC on Si PV cell with metallic contact (blue), and highly tapered NRA (black). The bump at 900 nm is due to detector change during data collection.

Sample	*a* (nm)	*b* (nm)	*c* (nm)	*l* (nm)	*h* (μm)	R_w (%)
Flat top	51	51	40	NA	0.95	12.2
Tapered	18	53	120	210	1.7	13.6
Highly tapered	10	45	100	330	1.5	6.6
Sol-gel	NA	NA	NA	NA	0.55	30.3
SLARC	NA	NA	NA	NA	0.08	7.8

Table 1: Measured nanorod parameters and R_w values for ZnO NRA and other ARCs. The non-tapered region volume fraction *f* was found to be ~ 0.7 for all NRAs.

Simulations

Since different synthesis conditions simultaneously changed several parameters in the resulting NRA ARCs (Table 1), to isolate the contribution of each nanorod parameter (*a*, *c*, *l*, or *f*) to the performance of the ARCs, we employed RCWA to calculate the front hemispherical reflectance spectra from the extracted nanorod parameters (Table 1) by systematically varying the value of one parameter while holding the other parameters to their default extracted values (Table 1). RCWA is a rigorous methodology for structures periodic in one or two dimensions that computes the electromagnetic modes present in each layer, then applies boundary conditions between the layers to calculate reflected and transmitted orders.[24] Optical constants for ZnO from literature were used for the calculations.[25] For RCWA, we subdivided each NRA into twelve layers: a bottom fused layer with $f = 1$, a non-tapered NRA layer with $f = 0.7$, and a 10-layer stack for the tapered region. To approximate the tapering of each NRA, we calculated diameter *d* and *f* for each layer in the stack using linear interpolation of the bottom of the tapered region ($d = b$, $f = 0.7$) and the top of the tapered region ($d = a$, $f = 0.7\ a^2/b^2$). To approximate the SEM observations, we also determined the effect for a linear variation in *h* of 10% by calculating the

reflectance spectra for NRAs each with uniform length ranging from h – 10% to h + 10% at 0.5% increment, and then averaging the resulting 21 spectra. Distributions in *a* and *b* were not accounted for because they were folded into the average volume fraction for each layer in RCWA. Front hemispherical reflectance spectra for the RCWA simulations were performed using Grating Diffraction Calculator, a commercial package that runs in Matlab. By varying one parameter at a time, the RCWA calculated front hemispherical reflectance spectra and subsequently the corresponding R_w enable us to isolate the effect of each morphological factor.

We found that good agreement between calculated and experimental reflectance spectra can be achieved through the elimination of interference fringes via a combination of nanorod tip tapering ($a < b$) and variation in nanorod length *h*. With no tip tapering and no length variation, i.e. flat top NRAs with uniform length, the reflectance spectra of a flat top NRA exhibited very strong interference fringes of ~ 20% intensity (Fig. 4a, red). The introduction of length variation dramatically decreased the interference fringe intensity to ~ 5% (Fig. 4a, blue), similar to the experimental data (Fig. 4a, black). In addition, for the flat top NRA, the R_w value from experiment of 12.2% (Table 1) is very close to the value from RCWA of 12.5% (Table 2). Further increase in length variation to 20% did not significantly change the strength of the interference fringes (Supporting Information). Thus, there is very good agreement between measured response and RCWA results for the flat top NRA.

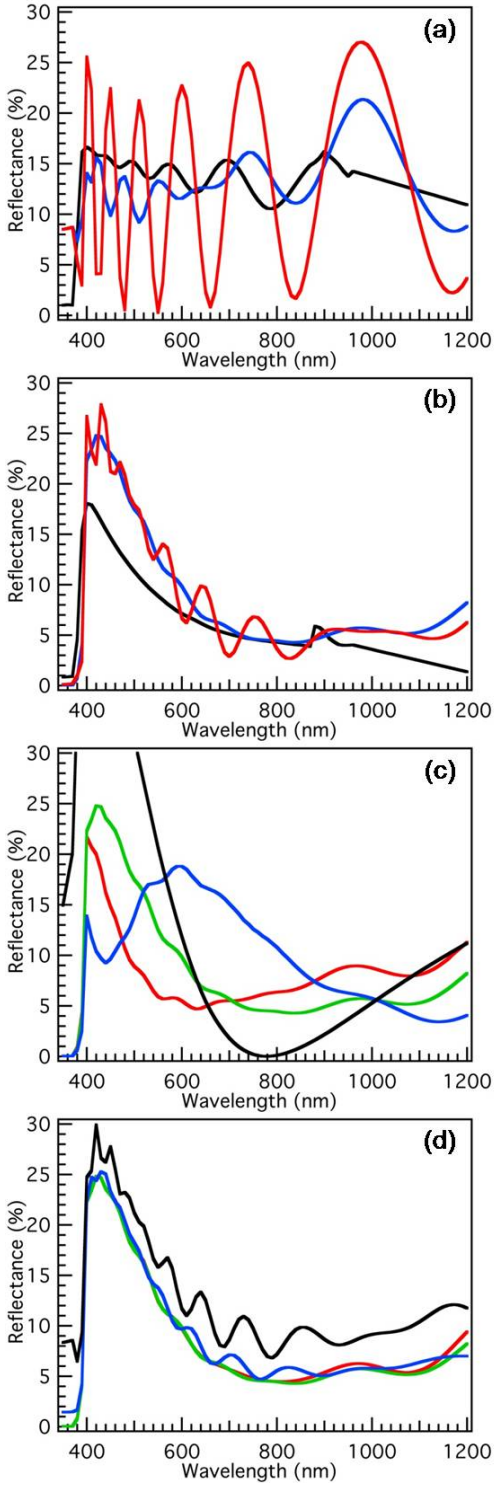

Figure 4: Effect of ZnO nanorod morphology on reflectance spectra of NRA ARCs calculated via RCWA. a) Flat top NRA with uniform length (red), 10% length variation (blue), and experimental data (black). b) Highly tapered NRA with uniform length (red), 10% length variation (blue), and experimental data (black). c) Highly tapered NRA with bottom layer thickness *c* of 75 nm (red), 100 nm (green), 150 nm (blue), and 100 nm ZnO SLARC (black). d) Highly tapered NRA with tip diameter *a* of 2 nm (red), 10 nm (green), 30 nm (blue), and 45 nm (black).

a (nm)	b (nm)	c (nm)	l (nm)	h (μm)	R_w (%)
2	45	100	330	1.5	**9.2**
4	45	100	330	1.5	**9.1**
10	45	100	330	1.5	**9.0**
20	45	100	330	1.5	**9.0**
30	45	100	330	1.5	**9.5**
45	45	100	330	1.5	**12.5**
10	45	**75**	330	1.5	**7.5**
10	45	**90**	330	1.5	**8.1**
10	45	**100**	330	1.5	**9.0**
10	45	**125**	330	1.5	**11.3**
10	45	**150**	330	1.5	**12.7**

Table 2: Effect of variation of one nanorod parameter on R_w values derived from RCWA spectra for highly tapered ZnO NRA ARC (f = 0.7). Parameters that are varied and the resulting R_w are in bold.

According to RCWA, tapering of the nanorod tips also contribute to suppression of interference fringes in the reflectance spectra. For example, a highly tapered NRA (a = 10 nm, Table 1) with uniform length exhibited interference fringes with intensity of ~ 4% (Fig. 4b, red), much lower than the flat top rods (Fig. 4a, red). The addition of a 10% length variation to this system reduced the interference fringe intensity to < 1% (Fig. 4b, blue), similar to the experimental data which showed no interference fringes (Fig. 4b, black). While both experimental and calculated spectra for the highly tapered NRA showed qualitative agreement in that both spectra monotonically decreased as wavelength increased (Fig. 4b), they exhibited significantly different R_w values of 6.6% (Table 1) and 9.0% (Table 2), respectively. This indicates that the tapering of the ZnO nanorods results in a more complex shape than our model of a linear decrease in diameter, preventing us from a quantitative comparison between experiment and theory. Nevertheless, we believe our model captures enough details of the experimental system to predict the effect of changing one parameter at a time, as shown below.

We found the shape of the reflectance spectra to be strongly influenced by c, the thickness of the fused ZnO bottom layer (Fig. 4c). By changing c from 75 nm to 100 nm while keeping the other parameters constant for a highly tapered NRA, the wavelength of reflectance minimum λ_{min} shifted from 600 nm (Fig. 4c, red) to 800 nm (Fig. 4c, green). A further increase in c to 150 nm shifted λ_{min} out of the experimental wavelength range and introduced a maximum in reflectance at 600 nm (Fig. 4c, blue). This behavior is similar to that of a SLARC ($\lambda_{min} = 4\ n\ c$) for n = 2, which matches the refractive index of dense ZnO at 633 nm; however, as we noted before, the reflectance spectra of NRA ARCs are less wavelength dependent than that of a SLARC, such as a 100 nm thick ZnO film (Fig. 4c, black). R_w derived from RCWA spectra for c between 75 nm and 150 nm increased from 7.5% to 12.7% (Table 2), suggesting that tailoring the fused layer thickness may be important in optimizing ARC performance. In short, both experimental data and RCWA calculations indicate that a tapered ZnO NRA with a fused bottom layer behaves like a modified SLARC with greater broadband suppression of reflection, particularly for the longer wavelengths.

A noticeable improvement of the ARC performance can be achieved with a moderate degree of nanorod tip tapering, according to RCWA calculations. When *a* was decreased from 45 nm, i. e. flat top nanorods (Fig. 4d, black), to 30 nm (Fig. 4d, blue), the reflectance spectra shifted downward across the entire wavelength range, and the interference fringes also decreased in intensity. Further reductions in the tip diameter to 10 nm (Fig. 4d, green) and 2 nm (Fig. 4d, red) eliminated the interference fringes while maintaining the overall shape of the reflectance spectra. From the corresponding R_w, we found that decreasing *a* to 30 nm improved R_w from 12.5% to 9.5%, and further reductions in tip diameter only resulted in a 0.5% improvement in R_w (Table 2). We also examined the effect of *f* and *l* on NRA ARC performance, and found that they affected the reflectance spectra in minor ways (Supporting Information). In summary, through a systematic examination of the effect of nanorod morphology on the reflectance spectra of ZnO NRAs on Si, we demonstrated that variation in nanorod length, thickness of the fused bottom layer, and tapering of nanorod tips all contribute to the improvement of ZnO NRA ARC performance by introducing broadband suppression of reflectance and eliminating interference fringes. These findings are in agreement with prior explorations of the idealized refractive index gradient of structured antireflection coatings.[26] The tapered nature of the ZnO NRAs leads to an impedance matching of the silicon to the air through a gradual reduction of the effective index away from the surface, and behave similarly to lithographically patterned sub-wavelength textured dielectric ARCs operating in the mid-infrared when the rod diameter is scaled to the wavelength.[27] By using aqueous solution synthesis of tapered ZnO NRAs, we demonstrated simple, large area fabrication of sub-wavelength textured ARCs for visible-near IR wavelengths, which would otherwise require complicated techniques such as e-beam or nanoimprint lithography followed by etching. Through modifications of NRA synthesis, in particular to tailor the bottom layer thickness and to further control nanorod shape, we may be able to further optimize the refractive index gradient and thus decrease reflectance.[26]

Summary

We fabricated textured ZnO ARCs via low temperature aqueous solution deposition of highly aligned ZnO NRAs. By controlling the solution growth conditions, we tuned the morphology of the ZnO NRAs, and showed that presence of a bottom fused layer combined with tapering of nanorod tips resulted in broadband suppression of reflectance, with R_w of 6.6% for a 1.5 μm highly tapered ZnO NRA. RCWA calculations of the effect of various nanorod parameters on ARC performance suggested that the highly tapered ZnO NRA ARC behaved like a modified SLARC with reduced wavelength dependence due to the nanoscale morphology, because the tapering produces impedance matching between Si and air through a gradual reduction of the effective refractive index away from the surface. Variation in nanorod length, presence of a fused ZnO base layer, and introduction of tip tapering all contributed to the decrease in reflectance and the elimination of interference fringes, in good qualitative agreement with experimental results. Due to the low temperature and substrate independent processing, these novel textured ZnO ARCs may be suitable for low cost, large area PV devices and other antireflection applications.

Supporting Information

All chemicals were purchased from Aldrich or Acros and used as received. 2.5 cm x 1.25 cm pieces of *N*-type Si(100) (Allied Bendix) were cleaned sequentially in soap solution (Aquet), water, acetone (with sonication, 10 min), methanol, and with UV ozone (UVO-Cleaner, Jelight, 20 min). For seeding, each substrate was coated with 15 μL of a 5 mM zinc acetate dihydrate solution in ethanol for 25 s and rinsed with ethanol. The coating was repeated four additional times, and the seed layer was annealed in a box furnace (Lindberg) in air at 350 °C for 20 min. Each substrate was placed at a ~ 30° angle to horizontal in a glass vial containing 12 mL of growth solution with zinc nitrate (ZN), hexamethylene tetraamine (HMT), and 1,3-diaminopropane (DAP). Each solution was heated to either 60 C or 92.5 C for various amounts of time, as detailed in Table S1. For sol gel deposited ZnO, a sol containing 1.5 M zinc acetate and 1.5 M ethanolamine in 2-methoxyethanol was spin coated on a Si substrate at 2000 rpm for 60 s, and pyrolyzed on hot plate at 300 ºC for 10 min. The spin coating/pyrolysis was repeated four additional times, and the sample was annealed in an oven at 600 ºC for 1h. The entire procedure was repeated once to yield a post-anneal film thickness of 0.55 μm.

Sample	T (°C)	[ZN] (mM)	[HMT] (mM)	[DAP] (mM)	Time (min)
Flat top	92.5	25	25	0	125 + 125
Tapered, 30 min	92.5	25	25	190	30
Tapered, 45 min	92.5	25	25	190	45
Tapered, 75 min	92.5	25	25	190	75
Tapered, 100 min	92.5	25	25	190	100
Hi. taper, 190 mM, 1 step	60	20	20	190	1080
Hi. taper, 190 mM, 2 step	60	20	20	190	1080
Hi. taper, 125 mM, 1 step	60	20	20	125	1080
Hi. taper, 125 mM, 2 step	60	20	20	125	1080

Table S1: Growth conditions for various ZnO NRAs. The flat top sample was placed in fresh solution after 125 min and grown for an additional 125 min to yield a length of 950 nm. The highly tapered, 2 step samples uses flat top rods grown for 125 min as seed layer.

The morphology and antireflection response of ZnO NRAs synthesized with 190 mM DAP at 92.5 °C can be tuned with further increases in growth time. For example, a growth time of 75 min increased the average nanorod length and diameter to 2.65 μm and 65 nm respectively (Fig. S1a), and a growth time of 100 min resulted in average nanorod length and diameter of 3.8 μm and 90 nm (Fig. S1b). In addition, the nanorod tips became more strongly faceted as growth time increased, leading to a more abrupt change in refractive index as a function of distance from the tip. Interestingly, the two NRAs exhibited almost identical reflectance spectra (Fig. S1c), suggesting that further increases growth time will not improve ARC performance.

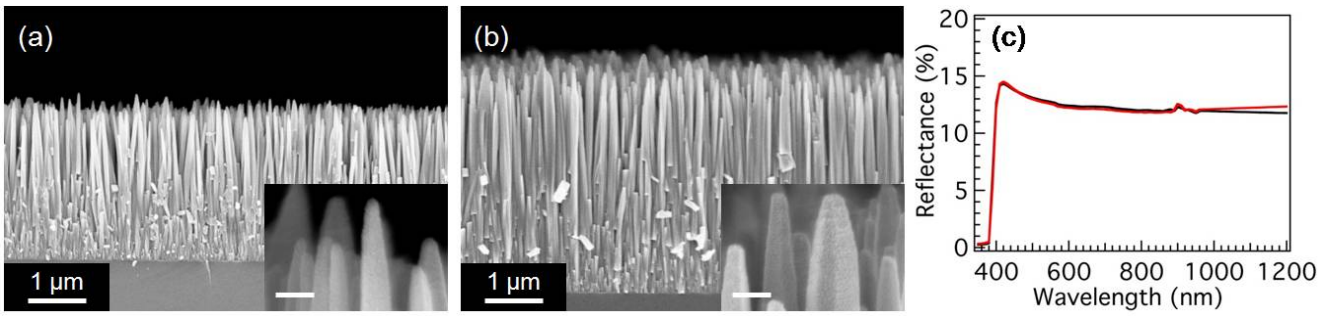

Figure S1: Morphology and ARC response of ZnO NRAs grown at 190 mM DAP and 92.5 °C for longer times. a) SEM image, 75 min. b) SEM image, 100 min. Inset, high magnification view of the samples (scale bar, 100 nm). c) Reflectance spectra of sample in S1a (black) and S1b (red), showing nearly identical response.

We also modified the ZnO NRA morphology by varying other growth parameters such as concentration of DAP and number of growth steps. For example, decreasing the DAP concentration to 125 mM at 60 °C increased the average nanorod length and diameter to 3.7 µm and 78 nm after 18 hours (Fig. S2a). NRAs were also synthesized via a two step growth process, where the seeded substrates were submerged in 20 mM ZN, 20 mM HMT solution without DAP at 92.5 °C for 125 min to create 500 nm long flat top nanorods, and then transferred to a 20 mM ZN/20 mM HMT solution with various DAP concentrations at 60 °C for 18 hours to yield tapered nanorods. Interestingly, two step growth using 190 mM (Fig. S2b) and 125 mM DAP (Fig. S2c) resulted greater *c* and smaller *l* compared to their one step counterparts, but other dimensions are quite similar (Table S2). All highly tapered NRAs have qualitatively similar reflectance spectra (Fig. S2d), with the 190 mM DAP, 1 step sample having the lowest R_w (main text).

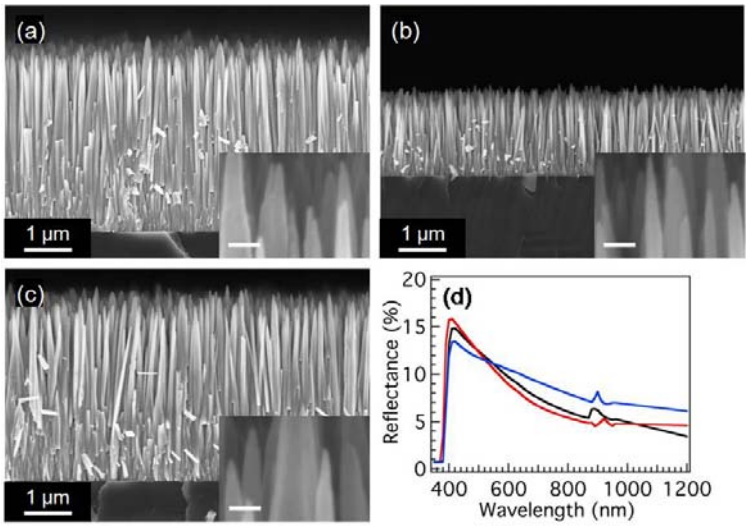

Figure S2: Morphology and ARC response of ZnO NRAs grown 60 °C. a) SEM image, 125 mM DAP, 1 step. b) SEM image, 190 mM DAP, 2 step. c) SEM image, 125 mM DAP, 2 step. Inset, high magnification view of the samples (scale bar, 100 nm). c) Reflectance spectra of sample in S2a (black), S2b (red), and S2c (blue).

When the nanorod parameters of the tapered ZnO NRAs are compared to their reflectance spectra and R_w values, several trends emerge in addition to those discussed in the main text (Table S2). First, increasing the length h of tapered NRAs slightly improved ARC performance, and for lengths greater ~ 2.5 μm, the calculated R_w value stabilized at 12.2% (Table S2). However, when the data for all NRAs are also included, a plot of R_w versus h shows no trend (Fig. S3a). Second, the highly tapered samples generally have smaller values for diameter a and also exhibited lower values R_w (Table S2). On the other hand, a plot of R_w versus a, while showing some clustering of data, does not exhibit a clear trend (Fig. S3b). Both results suggest that fine details in the nanorod tapering may play a more important role in determining the reflectance properties of the NRA ARCs.

Sample	a (nm)	b (nm)	c (nm)	l (nm)	h (μm)	R_w (%)
Flat top	51	51	40	NA	0.95	12.2
Tapered, 30 min	NA	45	35	NA	0.75	14.3
Tapered, 45 min	18	53	120	210	1.70	13.6
Tapered, 75 min	24	66	170	220	2.65	12.3
Tapered, 100 min	27	90	210	280	3.70	12.2
High taper, 190 mM, 1 step	10	45	100	330	1.50	6.6
High taper, 190 mM, 2 step	8	52	130	260	1.55	7.7
High taper, 125 mM, 1 step	11	78	260	380	3.70	8.2
High taper, 125 mM, 2 step	10	79	330	330	3.65	9.2

Table S2: Extracted peak shape parameters and R_w from various ZnO NRAs.

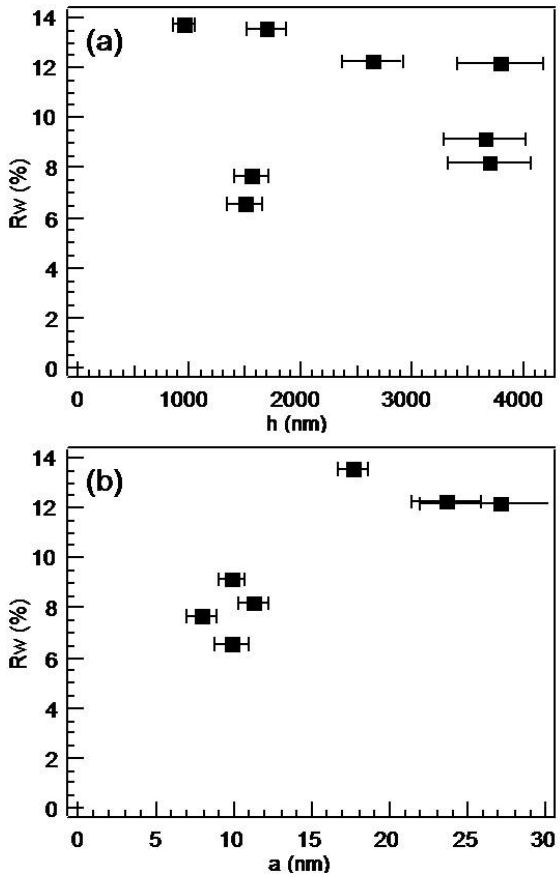

Figure S3: Weighted reflectance of ZnO NRAs as a function of nanorod parameters. a) Length *h*. b) Tip diameter *a*.

Using RCWA, we evaluated the effect volume fraction *f* and extent of tapered region *l* on the response of the NRA ARCs. Based on experimental data, the volume fraction of the ZnO NRA was measured to be 0.7. When the volume fraction of the non-tapered nanorod region was varied between 0.6 and 0.8, we observed only minor changes in the RCWA reflectance spectra (Fig. S4a). For example, the intensity of the interference fringes increased at $f = 0.8$ as the NRA approaches the hexagonal close pack limit for cylinders (0.906) (Fig. S4a, black). Because RCWA treats the non-tapered region as a solid film with an effective refractive determined by the volume fraction, and since there is minimal scattering in the substrate parallel direction due to the small nanorod diameter (45 nm), the weak dependence of reflectance on *f* is not surprising.

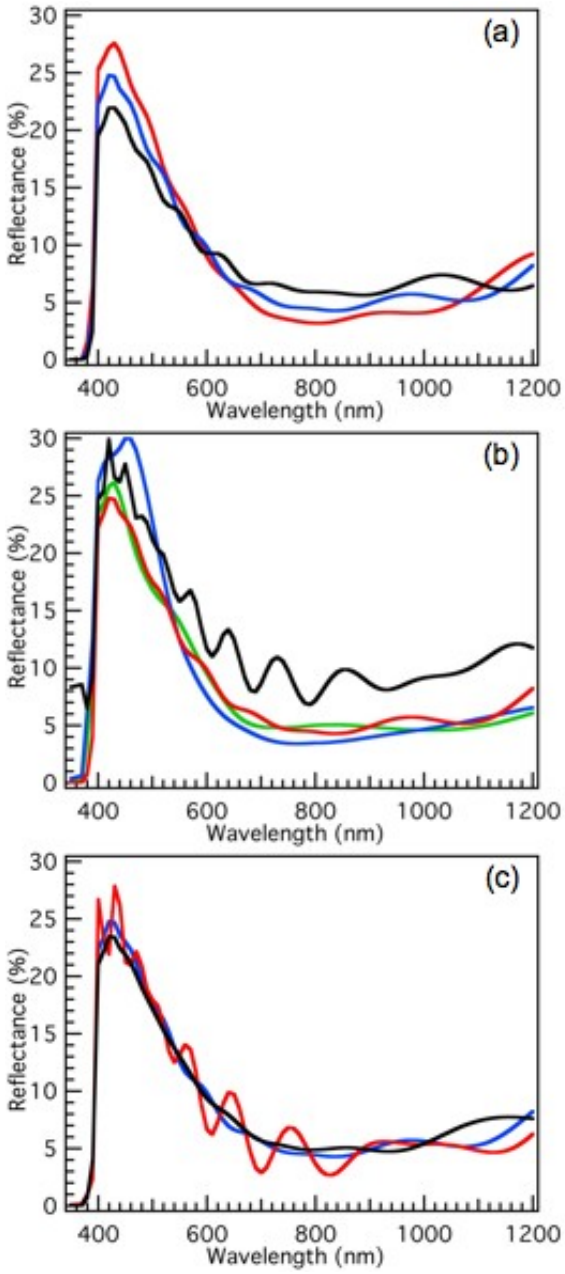

Figure S4: Effect of nanorod parameters on RCWA reflectance spectra. a) Non-tapered region volume fraction *f* of 0.6 (red), 0.7 (blue), and 0.8 (black). b) Extent of tapered region *l* of 0 nm (black), 330 nm (red), 1000 nm (green), and 1400 nm (blue). c**)** Variation in length *h* of 0% (red), 10% (blue), and 20% (black).

Compared to a non-tapered NRA with l = 0 nm (Fig. S4b, black), an increase in the extent of tapered region to 330 nm caused a broadband decrease in reflectance and the elimination of interference fringes (Fig. S4b, red), and the reflectance spectra remain unchanged with further increase of l to 1000 nm (Fig. S4b, green). When the tapering extended through the entire nanorod (l = 1400 nm, Fig. S4b, blue), we noted in an increase in reflectance below 550 nm and a decrease in reflectance at longer wavelengths. All values of l tested resulted in a reduction of R_w from 12.5% to ~ 9% (Table S3).

l (nm)	R_w (%)
0	12.5
330	9.0
400	8.9
1000	8.8
1400	9.2

Table S3: Effect of variation of tapered region extent l on R_w values derived from RCWA spectra for highly tapered ZnO NRA ARC (f = 0.7), with the other parameters at their default values of a = 10 nm, c = 100 nm.

As we mentioned in the main text, RCWA calculations showed that a variation in h of 10% or more suppressed the interference fringes of a highly tapered NRA with uniform length (Fig. S4c, red). Indeed, increasing the variation in h to 20% (Fig. S4c, black) resulted in a very similar reflectance spectra compared to a variation of 10% (Fig. S4c, blue), with very weak interference fringes of similar amplitude.

The weighted reflectance R_w was calculated using the equation

$$R_w = \frac{\int_{\lambda_1}^{\lambda_2} F(\lambda)\cdot IQE(\lambda)\cdot R(\lambda)\cdot d\lambda}{\int_{\lambda_1}^{\lambda_2} F(\lambda)\cdot R(\lambda)\cdot d\lambda} \qquad (1)$$

where $F(\lambda)$, $IQE(\lambda)$, and $R(\lambda)$ are photon flux, internal quantum efficiency, and reflectance as a function of wavelength, respectively. λ_1 = 350 nm and λ_2 = 1200 nm were used for our calculations. We derived $F(\lambda)$ from publicly available global solar spectral irradiance data (AM1.5) at http://rredc.nrel.gov/solar/spectra/am1.5/. We used external quantum efficiency spectra from a typical thin film multicrystalline solar cell to calculate $IQE(\lambda) = EQE(\lambda) / (1 - R(\lambda))$. A plot of $IQE(\lambda)$, $EQE(\lambda)$, and $F(\lambda)$ is shown in Figure S5.

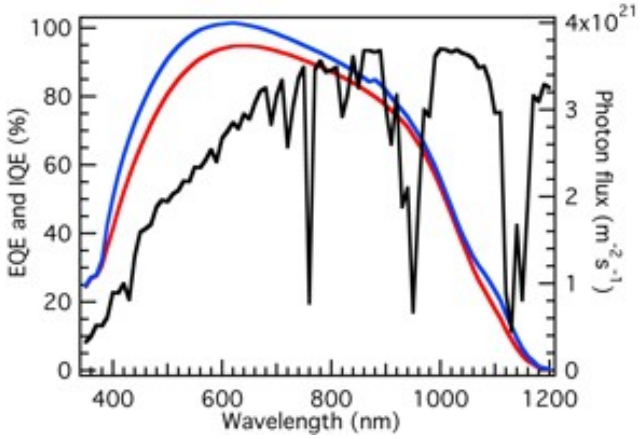

Figure S5: EQE (red) and IQE (blue) spectra of a typical thin film multicrystalline Si solar cell, and photon flux of terrestrial global solar illumination at AM1.5 (black).

References

M. A. Green, *Silicon Solar Cells: Advanced Principles and Practice* (Bridge, Sydney, 1995).

P. Lalanne and G. M. Morris, Nanotechnology **8**, 53 (1997).

Y. Kanamori, K. Hane, H. Sai, and H. Yugami, Appl. Phys. Lett. **78**, 142 (2001).

S. Koynov, M. S. Brandt, and M. Stutzmann, Appl. Phys. Lett. **88**, 203107 (2006).

C. H. Sun, B. Jiang, and P. Jiang, Appl. Phys. Lett., **92**, 061112 (2008).

C. C. Striemer and P. M. Fauchet, Appl. Phys. Lett. **81**, 2980 (2002).

S. H. Zaidi, D. S. Ruby, and J. M. Gee, IEEE Trans. Electron Devices, **48**, 1200 (2001).

D. S. Ruby, S. H. Zaidi, S. Narayanan, B. M. Damiani, A. Rohatgi, Solar Energy Materials and Solar Cells, **74**, 133 (2002).

D. S. Ruby, W. L. Wilbanks, and C. B. Fleddermann, in *Conference Record of the First WCPEC*, (IEEE, Piscataway, NJ, 1994), p. 1335.

K. Orgassa, U. Rau, Q. Nguyen, H. W. Schrock, and J. H. Werner, Prog. Photovolt. **10**, 457 (2002).

K. Ramanathan, M. A. Contreras, C. L. Perkins, S. Asher, F. S. Hasoon, J. Keane, D. Young, M. Romero, W. Metzger, R. Noufi, J. Ward, and A. Duda, Prog. Photovolt. **11**, 225 (2003).

H. Takato, M. Yamanaka, Y. Hayashi, R. Shimokawa, I. Hide, S. Gohda, F. Nagamine, and H. Tsuboi, Jpn. J. Appl Phys. **31**, L1665 (1992).

P. Doshi, G. E. Jellison, and A. Rohatgi, Appl. Opt. **36**, 7826 (1997).

A. G. Aberle, Sol. Ene. Mat. Sol. Cel. **65**, 239 (2001).

B. S. Richards, Prog. Photovolt. **12**, 253 (2004).

S. R. Kennedy and M. J. Brett, Appl. Opt. **42**, 4573 (2003).

B. S. Richards, S. F. Rowlands, C. B. Honsberg, and J. E. Cotter, Prog. Photovolt. **11**, 27 (2003).

J.-Q. Xi, M. F. Schubert, J. K. Kim, E. F. Schubert, M. Chen, S.-Y. Lin, W. Liu, and J. A. Smart, Nat. Photon. **1**, 176 (2007).

L. E. Greene, M. Law, D. H. Tan, M. Montano, J. Goldberger, G. Somorjai, and P. Yang, Nano. Lett. **5**, 1231 (2005).

Y.-J. Lee, T. L. Sounart, D. A. Scrymgeour, J. A. Voigt, and J. W. P. Hsu, J. Cryst. Gro. **304**, 80 (2007).

T. L. Sounart, J. Liu, J. A. Voigt, J. W. P. Hsu, E. D. Spoerke, Z. R. Tian, and Y. Jiang, Adv. Func. Mater. **16**, 335 (2006).

Y.-J. Lee, T. L. Sounart, J. Liu, E. D. Spoerke, B. B. McKenzie, J. W. P. Hsu, and J. A. Voigt, Cryst. Growth Des., in review.

M. Ohyama, H. Kozuka, and T. Yoko, Thin Solid Films **306**, 78 (1997).

M. G. Moharam and T. K. Gaylord, J. Opt. Soc. Am. A. **3**, 11 (1986).

H. Yoshikawa and S. Adachi, Jap. J. Appl. Phys. **36**, 6237 (1997).

W. H. Southwell, J. Opt. Soc. Am. A **8**, 549 (1991).

D. S. Hobbs and B. D. MacLeod, Proc. SPIE **5786**, 349 (2005).

Effect of polymer processing on the performance of poly(3-hexylthiophene) / ZnO nanorod photovoltaic devices

Introduction

Organic photovoltaic (OPV) devices based on nanostructured composites of electron donor and acceptor materials promise to deliver future solutions to low-cost energy generation.[2] Bulk heterojunction devices based on polymer-fullerene blends already demonstrate power conversion efficiencies exceeding 5%.[3-8] Such devices can be printed using roll-to-roll compatible techniques while maintaining high efficiencies.[9,10] However, control of the blend morphology is determined by solvent selection and annealing processes that must be optimized for each donor-acceptor combination.[5,7,8] Other electron acceptor materials have been investigated in hopes of improving charge transport. Bulk heterojunction devices made of polymer-metal oxide nanoparticle blends have been shown to be reasonably efficient.[11-13] However, the morphology of the composite system can be more deliberately controlled by employing nanoporous metal oxide acceptors that are deposited directly on the substrate and subsequently filled with a conjugated polymer donor.[14,15] In addition to improved electron mobility associated with ordered metal oxide nanostructures, the hole mobility of the conjugated polymer could be enhanced in the direction normal to the substrate by infiltrating the polymer into a nanoporous metal oxide film with vertically oriented pores, due to an alignment of the polymer chains along the walls of the pores.[16] Arrays of zinc oxide (ZnO) nanorods are a particularly well suited to this application as they can be grown normal to the substrate using low temperature hydrothermal growth, have excellent electron mobilities, and have a rod-to-rod spacing that is compatible with the short exciton diffusion lengths (< 10 nm) found in conjugated polymer donor materials.[17-19] Results on hybrid polymer-ZnO nanorod composite devices have yet to demonstrate increased performance over blend devices,[20-23] in part due to the lack of optimized device structures and processing.

The infiltration of the polymer into the nanostructured metal oxide is of particular importance for optimizing the performance of these hybrid devices with small rod-to-rod spacings. Previous studies on polymer/ZnO nanorod composites have employed ZnO arrays with large pore sizes (~100 nm) due to the disordered orientation of the nanorods.[20,22,23] As such, these devices have not employed extensive infiltration methods beyond spin coating the polymer on the ZnO nanorod arrays. In a previous publication, we have demonstrated excellent control in the synthesis of ordered ZnO nanorod arrays resulting in less than 20 nm spacing between the rods.[24] Such arrays should provide a near ideal architecture for an ordered organic-inorganic based bulk heterojunction device.[14,15] The purpose of this paper is to investigate how different poly(3-hexylthiophene) (P3HT) infiltration techniques affect the performance of solar cell devices based on these densely ordered ZnO nanorod arrays. In particular, we report on the effect of solvent selection and annealing conditions.

Materials and Methods

Sample Preparation. Devices were fabricated on patterned indium tin oxide (ITO) coated glass substrates. The sheet resistance of the ITO was 13 $\wedge$/cm^2 (Colorado Concept Coatings LLC). The 1”x1” substrates were cleaned by ultrasonic agitation in dichloromethane (10 min), acetone

(10 min), rinsing with methanol, and then exposed to an UV-ozone treatment (UVO-Cleaner, Jelight) for 20 min. A ZnO seed layer was deposited from a 5 mM solution zinc acetate dihydrate (Aldrich) in ethanol and annealed at 350 °C for 20 minutes to form a ZnO film as described previously.[24,25] ZnO nanorods were subsequently grown from the seeded substrate placed facing down in 24 mL of a solution containing 25 mM zinc nitrate (Aldrich) and 25 mM hexamethylenetetramine (HMT) at 92.5°C for 75 minutes. The samples were then rinsed with DI water and dried in air. The resulting ZnO nanorods were ~ 200 nm in length and ~ 45 nm in diameter. By varying growth time, nanorods of different lengths can be grown. Planar ZnO films were also fabricated by spin coating at 2000 RPM from a 0.75M zinc acetate dihydrate in 2-methoxyethanol with a 1:1 ratio of zinc acetate to ethanol amine. The sol-gel film was subsequently annealed on a hot plate in air at 300 °C for 10 minutes after which the film was rinsed with DI water, acetone, and isopropanol. According to x-ray diffraction measurements, the ZnO nanorod arrays were very well oriented with the (0001) direction normal to the substrate. The sol-gel ZnO films were polycrystalline, but highly (0001) textured.

Poly(3-hexylthiophene) (P3HT) was used as purchased from Rieke Metals. Prior to depositing the P3HT, the ZnO films were heated on a hot plate at 150 °C in air for 30 minutes followed by cooling under flowing N_2. Immediately after this process, the samples were placed on the spin coater and the P3HT films were deposited. Films were spin coated from solutions of P3HT either dissolved in chloroform at a concentration of 20 g/L and spin speed of 800 RPM, or in 1,2-dichlorobenzene at 40 g/L and 600 RPM, both for 60 seconds. The samples spin coated from dichlorobenzene were then placed in covered glass Petri dishes and allowed to dry over the course of 45 minutes. The dry samples were then used as deposited, or were subsequently annealed at 150 °C and 225 °C in a nitrogen atmosphere to enhance polymer infiltration. The annealing time at 150 °C was 10 minutes. When heated to 225 °C, the polymer was melted and then allowed to cool slowly for ~ 45 minutes to help to re-crystallize the polymer. Finally, silver electrodes were thermally evaporated at a pressure of 8×10^{-7} torr with a total thickness of 100 nm. The resulting device area was 0.1 cm^2.

Sample Characterization. UV-vis absorption spectra were measured using an Ocean Optics, Inc. USB-ISS-UV/VIS with a USB 2000 spectrometer. X-ray diffraction data were collected on a Bruker D-8. The morphology of the ZnO nanorods and the P3HT/ZnO nanorod composites was characterized using a Zeiss field-emission source scanning electron microscope (SEM). The samples were prepared for cross-sectional SEM by scoring the substrate, cooling them in liquid nitrogen, and cleaving the cold substrates to obtain a clear cross-section. The current density-voltage (J-V) response of the devices was measured with a Keithley 238 high current source power meter on a Spectrolab XT-10 solar simulator, which was calibrated for AM1.5 illumination with a light intensity of 100 mW/cm^2 using a reference Si solar cell. The external quantum efficiency (EQE) spectra were measured using a calibrated Si photodiode with a spot size smaller than the device area and an intensity of 2 μW at 520 nm. The photoconductivity of the polymer, nanorods, and composites were measured using the contactless time-resolved microwave conductivity (TRMC) technique as described previously.[18,26,27] In brief, the change in microwave power absorbed by the sample can be directly related to the photoinduced conductance, ΔG, of the films by $\frac{\Delta P}{P} = -K\Delta G$, where K is an experimentally determined calibration factor derived from the resonance characteristics of the cavity and the dielectric properties of the

samples used. Since charge carriers will be generated during the pulse and eventually decay, ΔG will be time dependent and referred to as 'photoconductance transient'. The instrument response is ~ 10 ns, limited by the response time of the microwave cavity. The End-of-Pulse photoconductance, ΔG_{EOP}, is related to the product of the quantum yield for mobile charge carrier generation per absorbed photon under our 5 ns long pulses (ϕ) and the sum of their mobilities ($\Sigma\mu$) by $\varphi\Sigma\mu = {}^{\Delta G_{EOP}}\!/_{I_0 F_A \beta q_e}$, where I_0 is the incident photon flux, F_A the fraction of incident light absorbed by the film, β is the ratio between the broad and narrow inner dimensions of the waveguide used (2.08 in this case) and q_e the elementary charge.[18,26-28] For the TRMC measurements on P3HT or P3HT/ZnO nanorod composites the polymer was pumped with 500 nm laser pulses, while measurements on the ZnO nanorods were carried out under excitation with 300 nm pulses.

Results and Discussion

Past studies on P3HT/ZnO-based devices have relied on polymer films spin coated from chloroform or chlorobenzene on disordered ZnO nanorod arrays.[20,22,23] Here we first examine the choice of solvent on the infiltration of P3HT into dense, ordered ZnO nanorod arrays. Figure 1 shows the dramatic effect of solvent selection. When spin coating the P3HT films from chloroform on top of ordered ZnO nanorod arrays, there is very poor infiltration of the polymer into the pore structure of the ZnO arrays, as seen in Figure 1(a). Clearly the wetting of the ZnO structures by the P3HT is poor, resulting in a void space on top of the ZnO rods. It has been reported that increased film drying time can enhance the molecular ordering and, therefore, the carrier mobility in P3HT/fullerene blends.[5,29] In these blends, films spin coated from dichlorobenzene were allowed to dry in covered Petri dishes over the course of 20 minutes. Here, we have employed the solvent annealing process through the use of dichlorobenzene, a high boiling point, low vapor pressure solvent, to more effectively infiltrate P3HT into ZnO nanorod arrays. Figure 1(b) shows that the infiltration of the P3HT spin coated from dichlorobenzene is greatly enhanced. To gauge the amount of polymer that was effectively infiltrated into the small pores in the ZnO nanorod array, we removed any polymer not infiltrated by soaking the composites in chloroform for 10 seconds and rinsing with more chloroform.[30] The polymer not infiltrated was immediately dissolved and the infiltrated polymer remained in the pores even after long exposures (~ 5 min.) or multiple soak/rinse cycles. The optical density increased from 0.1 to 0.15 when changing solvents from chloroform to dichlorobenzene. Cross sectional SEM images of the rinsed devices are presented in Figure 1(c,d). Figure 2 compares the optical absorption spectra for P3HT/ZnO nanorod composites with P3HT spin coated from chloroform and dichlorobenzene. The shoulders due to vibronic transitions in the UV-vis spectra of the dichlorobenzene films were enhanced, as interpreted by the increased shoulders at 550 and 600 nm. Previous thin film transistor work has shown that the presence of these shoulders correlates to enhanced hole mobility in the polymer.[31-33] Thus, the increased molecular order observed in blend devices prepared from dichlorobenzene solutions was also observed in these P3HT/ZnO nanorod composites.

As seen in Fig. 1a, the P3HT forms a large gap with the top, polar (0001) surfaces of ZnO nanorods and wicks in among the non-polar (10$\bar{1}$0) surfaces.[34,35] The polarity of ZnO surfaces might be an additional complication to polymer infiltration. In previous ZnO nanorod/P3HT solar cell work, disordered and less dense ZnO nanorod arrays were used, which present the

polymer with more of the nonpolar surfaces of the ZnO nanorods and may help polymer intercalation through more favorable interfacial interactions. In this work, where well-oriented (vertical) ZnO nanorod arrays were used, P3HT largely was exposed to the top, polar surface of the ZnO, which might serve as a barrier to efficient polymer infiltration.

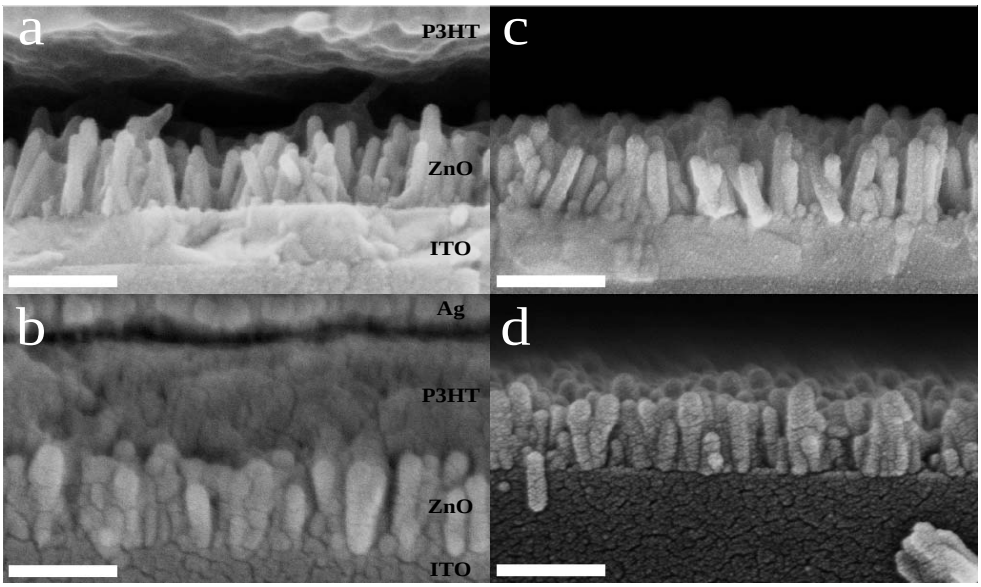

Figure 1. Cross sectional SEM images of P3HT/ZnO nanorod composite PV devices, for P3HT spin coated from chloroform (a) and with P3HT spin coated from 1,2-dichlorobenzene (b). Also shown are images after removing the polymer on top of the rods, chloroform (c), and 1,2-dichlorobenze (d). Scale bars: 200 nm.

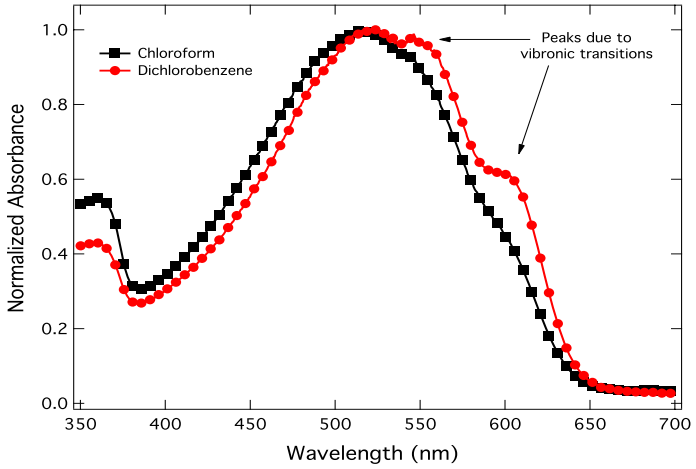

Figure 2. Normalized absorbance spectra for P3HT/ZnO nanorod composites with P3HT spin coated from chloroform (black squares) and with P3HT spin coated from 1,2-dichlorobenzene (red circles).
Figure 3 shows that the photovoltaic response of the dichlorobenzene devices is greatly enhanced. When switching from chloroform to dichlorobenzene, the open circuit voltage (V_{OC}) increased from 484 mV to 556 mV, the short circuit current density (J_{SC}) increased from 0.74 mA/cm^2 to 0.90 mA/cm^2, and the power conversion efficiency ( ) increased from 0.17% to 0.23%, as seen in Table 1. This is believed to be due to the increased infiltration of the polymer

into the ZnO nanorod structures as well as to enhanced carrier transport through the more ordered polymer phase. Therefore, the solvent selection and drying time (solvent annealing) have a dramatic effect on polymer infiltration, ordering, and consequently on the as-prepared P3HT/ZnO nanorod composite solar cell performance.

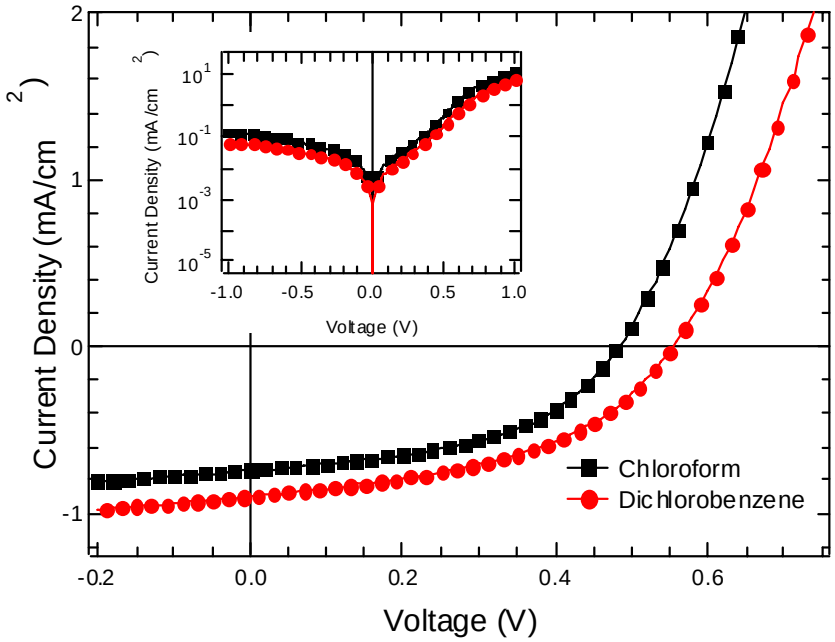

Figure 3. Current density vs. voltage (J-V) for illuminated (at AM 1.5) ITO/ZnO nanorod/P3HT/Ag devices with P3HT spin coated from chloroform (black squares) and with P3HT spin coated from 1,2-dichlorobenzene (red circles). Inset shows the dark J-V characteristics of the two devices.

Solvent	Temperature (°C)	V_{OC} (mV)	J_{SC} (mA/cm^2)	*FF* (%)	(%)
CF	NA	484	0.74	48.5	0.17
DCB	NA	556	0.90	45.8	0.23
DCB	150	438	1.24	46.6	0.25
DCB	225	443	1.33	48.4	0.28

Table 1. Photovoltaic properties of devices spin coated from chloroform (CF) and 1,2-dichlorobenzene (DCB). Devices were annealed at the temperature or were not annealed (NA) as indicated.

To further enhance the polymer infiltration and device performance, the effect of annealing of the P3HT/ZnO composites was studied. Following published work on melt infiltration of P3HT into mesoporous TiO_2 films with pore diameters of 6 nm,[1,30] we have employed a similar approach to facilitate the infiltration of the P3HT into the ordered ZnO nanorod arrays in this study. P3HT films were spin coated from dichlorobenzene onto ZnO nanorods. Figure 4a-c shows cross-sectional SEM images of ZnO/P3HT photovoltaic devices with as-made P3HT films (a) and those annealed at 150 °C (b) and 225 °C (c) under nitrogen. It is evident that the infiltration of the polymer was enhanced with increasing anneal temperature. It is important to note that the apparent loss in adhesion between Ag and P3HT in the sample annealed at 225 °C

(Figure 4c) is caused by the freeze-fracture process used to prepare cross-sectional specimens. The amount of infiltrated polymer can be estimated by optical absorption after rinsing the samples with chloroform to remove the uninfiltrated polymer on top of the rod arrays.[30] It is clear from cross sectional SEM images (Figure 4d-f) that more P3HT adhered to ZnO nanorods in the annealed samples. The optical density of the embedded P3HT increased from 0.15 to 0.25 after annealing at 150 °C, and to 0.95 after melt infiltration at 225 °C.

Figure 5 shows the best results we have obtained on P3HT/ZnO nanorod composite solar cells for each polymer annealing condition outlined above. The photovoltaic performance of the annealed P3HT/ZnO nanorod composites increased with annealing temperature, mainly due to the larger J_{SC}. The J_{SC} increased from 0.90 mA/cm^2 when not annealed, to 1.24 mA/cm^2 after annealing at 150 °C, and to 1.33 mA/cm^2 after annealing at 225 °C, as seen in Table 1. This increase in J_{SC} with annealing appears to correlate well with the enhancement in P3HT infiltration as discussed above. Improved polymer infiltration into the ZnO nanorod array increased the interfacial area of the device, leading to more efficient charge collection from the device. As a result the power conversion efficiency ( ) increased from 0.23% without annealing, to 0.25% after annealing at 150 °C, and to 0.28% after annealing at 225 °C. While the devices presented here showed that the V_{OC} decreased from over 550 mV to 440 mV after annealing at 150 °C or 225 °C, this trend is not consistently observed. Currently the variation in the V_{OC} is not yet fully understood and will be the subject of further investigation.

We observed through optical absorption data that when neat films of P3HT were cooled after melting (225°C anneal), the polymer chains became more disordered than as-prepared neat films made by slow drying from dichlorobenzene. This can be identified through loss of the shoulders due to vibronic transitions in the spectra at 550 nm and 600 nm. Therefore, to minimize the loss of molecular ordering when the P3HT in the ZnO nanorod device was heated at 225 °C, it was allowed to cool from the melt slowly over the course of 45 minutes in order to imitate the organization of the polymer chains when the films were dried slowly after being spun from dichlorobenzene. Though slow cooling increases the order in melt-processed films, we still observed a small loss in polymer chain ordering after cooling slowly from a melt (Figure 5 inset). Additionally, the melt processing erases the processing history, so that melt infiltrated films prepared from dichlorobenzene are identical to those made from chloroform.

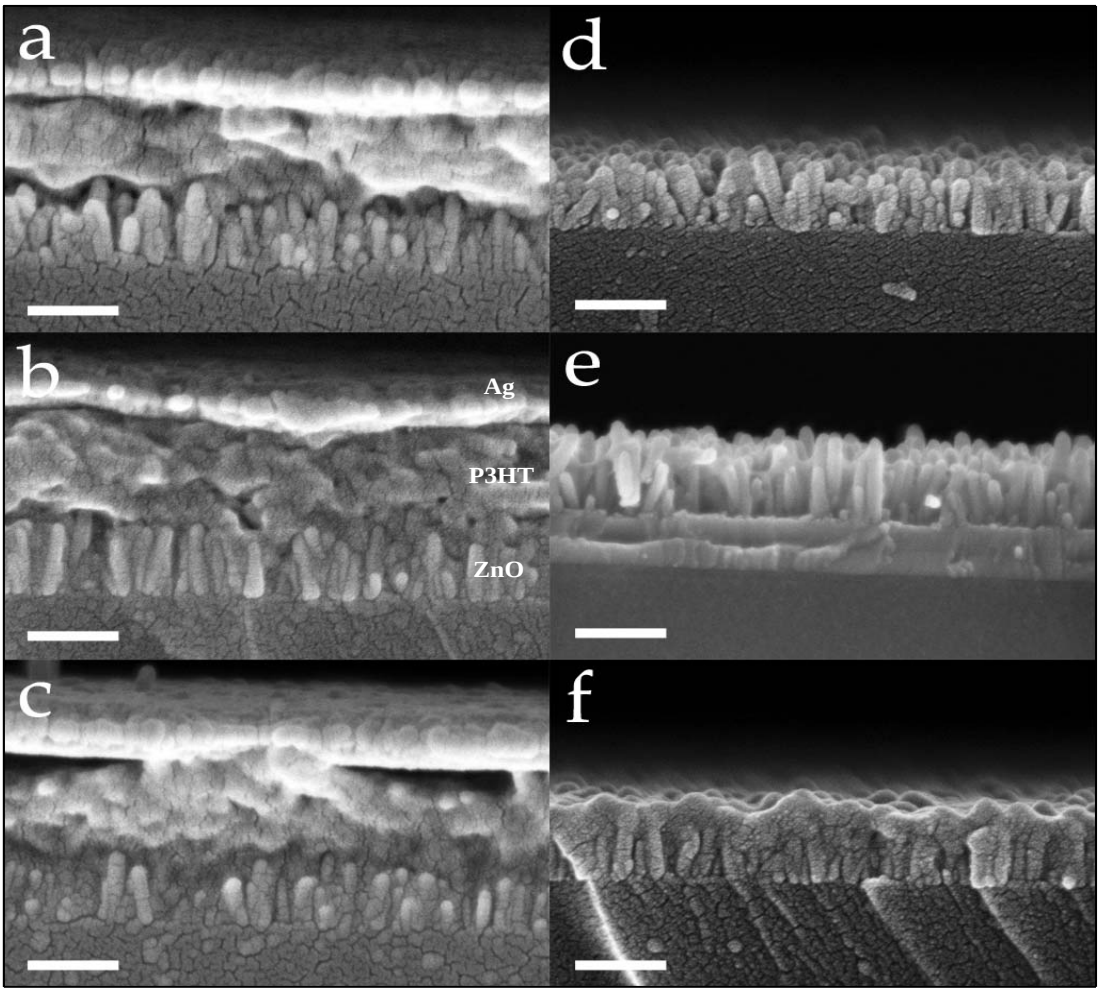

Figure 4. Cross sectional SEM images of P3HT/ZnO nanorod composite PV devices, without annealing (a), 150 °C (b), and 225 °C (c). Also shown are images after removing the polymer on top of the rods, no anneal (d), 150 °C (e), 225 °C (f). Scale bars: 200 nm.

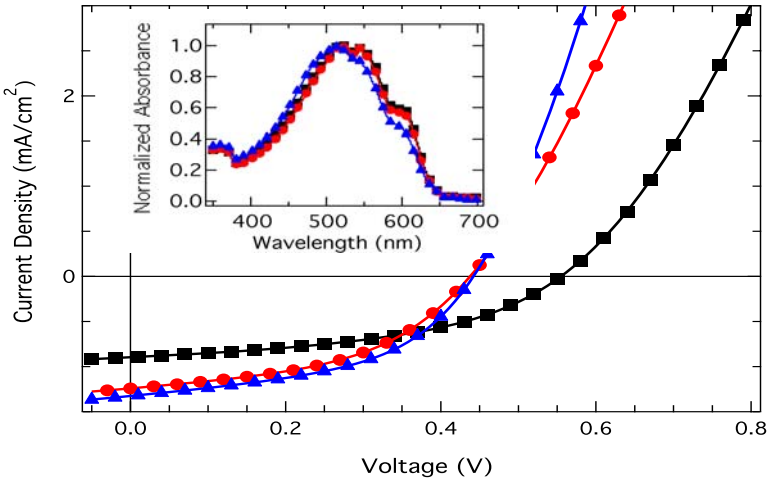

Figure 5. Best photovoltaics performance (illuminated at AM1.5) for ITO/ZnO nanorod/P3HT/Ag devices not annealed (black squares), annealed at 150 °C (red circles), and annealed at 225 °C (blue triangles). Inset shows normalized absorbance spectra of P3HT/ZnO nanorod devices not annealed (black squares), annealed at 150 °C (red circles), and annealed at 225 °C (blue triangles).

The improvement in device performance with annealing is also reflected in the external quantum efficiency (EQE) of the devices as seen in Figure 6. Here, we observed the same trend of increased photon to current conversion efficiency as a result of increased annealing temperature. Additionally, there was a small blue shift in the spectrum when the polymer was annealed at 225 °C, which was also observed through the loss of shoulders in the absorbance spectrum of the device (Fig. 5 inset). This leads to decreased overlap with the solar spectrum as well as reduced hole mobility, which would reduce the J_{SC} from what would be expected due to the enhanced polymer infiltration after annealing at 225 °C. Despite this, the device annealed at 225 °C demonstrated a higher J_{SC} than the other devices. This result points to a significant improvement in the infiltration of the P3HT or better electrical contact between P3HT and ZnO.

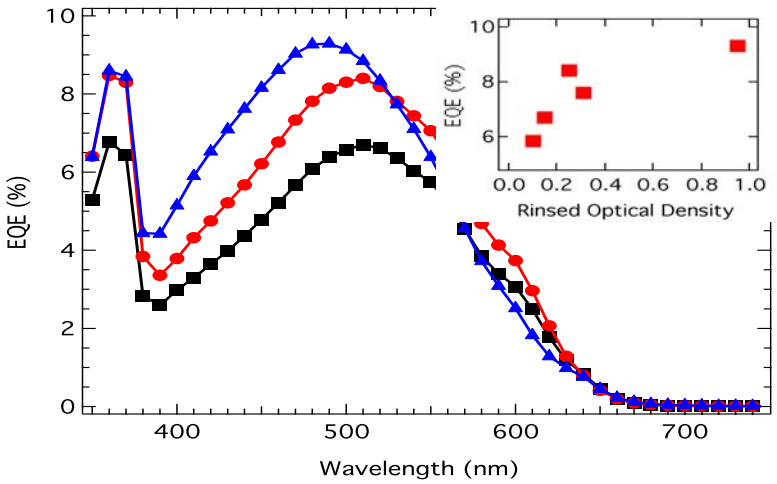

Figure 6. External quantum efficiency spectra of ITO/ZnO nanrod/P3HT/Ag devices not annealed (black squares), annealed at 150 °C (red circles), and annealed at 225 °C (blue triangles). Inset shows EQE vs. rinsed optical density of P3HT/ZnO rod composite devices.

Previous work on P3HT/mesoporous TiO_2 composites has demonstrated that the transport properties of the polymer were substantially diminished after melt infiltration.[1] In that work, when the optical density of the embedded polymer was increased, the device EQE was reduced. This was attributed to a filtering effect of the polymer infiltrated deepest into the porous TiO_2 structure, where the hole mobility of the polymer was too low to allow for efficient carrier transport from this region upon photoexcitation. Hence, the absorption of light by the deeply infiltrated polymer led to a reduction in the amount of light available for the active region of the device, which was closer to the hole-collecting electrode, without contributing to photocurrent. In contrast, the annealing results in our P3HT/ZnO nanorod composites show the opposite trend: the EQE, J_{SC}, and device efficiency all increase with increasing polymer infiltration. The inset in Figure 6 demonstrates that EQE increases with the amount of polymer infiltrated into the ZnO nanorod composite. These are data collected from a series of devices annealed at different infiltration temperatures as well as with devices based on 100 nm ZnO rods. The filtering effect is not observed and hole transport is not the primary limiting factor of the performance of P3HT/ZnO nanorod devices. The difference in the two systems is likely due to the size and ordering of the pores. The ordered ZnO nanorod arrays have a larger pore size of ~ 20 nm compared to the 6 nm pore size in the mesoporous TiO_2. In addition, the pores in the ZnO nanorod arrays used in this study are vertically aligned, which might help to reduce the amount of disorder that is induced in the P3HT by infiltration into the mesoporous TiO_2. This, in turn, might help to preserve intrinsic P3HT hole mobility and transport properties.

The effect of annealing was also investigated using TRMC. A comparison of the TRMC signal from the P3HT/ZnO nanorod and from P3HT only on glass is shown in Figure 7. The magnitude of the signal from the not annealed pure polymer is in good agreement with previous work.[27,28] In these films, which were spin coated from dichlorobenzene, we observed an increase in the TRMC signal only after melting from 225 °C. This could be attributed to a higher carrier generation yield in the bulk of the polymer,[27] which could compensate for a decreased hole mobility that would result from the polymer becoming less ordered as observed in the UV-vis spectra (Fig. 5 inset).

While the signal from pure P3HT is dominated by the hole density and mobility,[28] the signal from the P3HT/ZnO samples is dominated by the electron density and mobility in ZnO.[27,36] The magnitude of the TRMC signal for the P3HT/ZnO nanorod sample is higher than what has been reported previously for P3HT/ZnO nanoparticle blends[36] and P3HT/ZnO bilayers.[27] The difference is attributed to higher mobility in the ZnO nanorods compared to nanoparticles,[37] and, in the case of the P3HT/ZnO bilayers,[27] to the increased surface area of the ZnO nanorod film. A similar trend with regard to P3HT annealing was observed in the P3HT/ZnO nanorod composites, which might suggest that the same changes in P3HT after melting contributed to the increased TRMC signal observed in the composites.

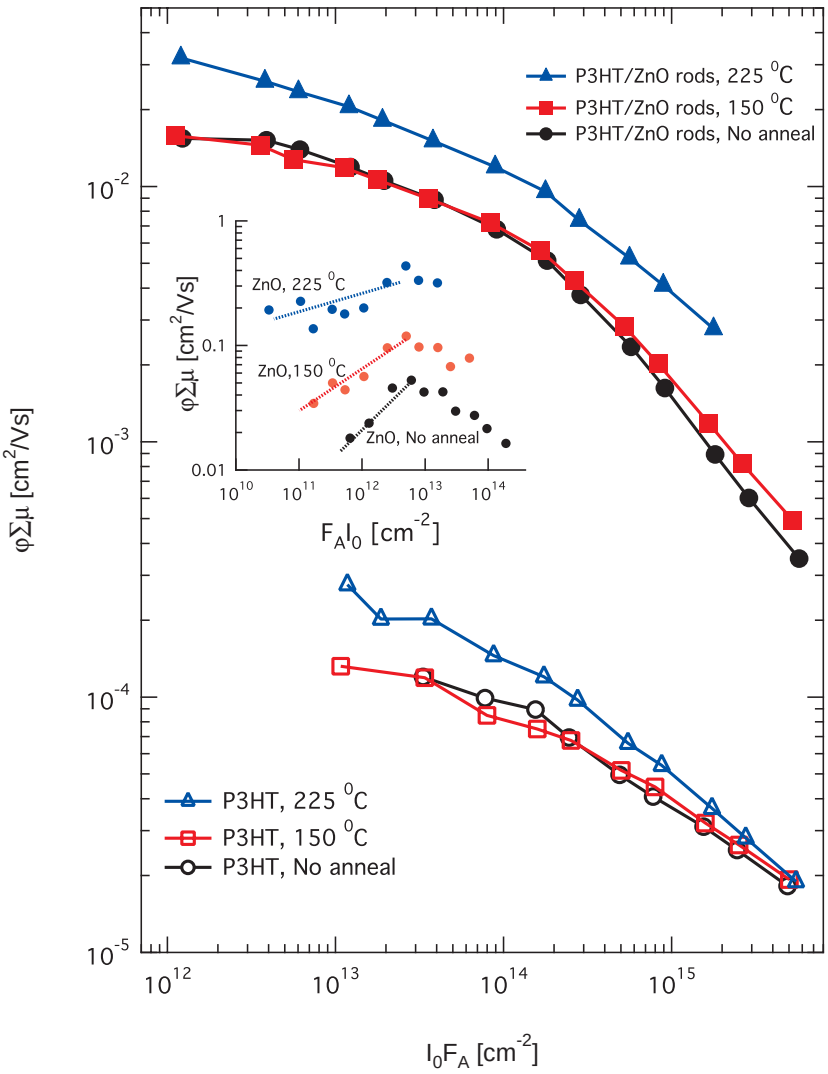

Figure 7. Photoconductivity per absorbed photon versus absorbed photon flux measured with TRMC under excitation with 500 nm pulses for P3HT (open symbols) and P3HT/ZnO rod composites (solid symbols), not annealed (black circles), annealed 150 °C (red squares), and annealed 225 °C (blue triangles). The inset shows photoconductivity per absorbed photon versus absorbed photon flux measured with TRMC under excitation with 300 nm pulses for the ZnO nanorods before annealing (black), annealed at 150 °C (red), and annealed 225 °C (blue). The lines are guides to the eye (see text).

In order to investigate changes of the transport properties of the rods themselves with annealing we carried out TRMC measurements of the rods without a polymer under excitation with 300 nm laser pulses. The results are shown in the Figure 7 inset. The light intensity dependence of the TRMC signal for the non-annealed ZnO nanorod sample resembles that of on TiO_2 nanoparticles.[26] At low light intensities a trap-filling regime is observed (highlighted with the dotted line). With annealing, the TRMC signal increases and exhibits a weaker dependence on light intensity in the trapping regime. These observations indicate that annealing removes traps from the ZnO nanorods, in much the same way that background illumination inactivates the traps in TiO_2.[26] While it is not possible to extract the exact dependence of the mobility of electrons in

the ZnO rods on annealing temperature, the data indicate that the mobility increases with annealing, consistent with previous reports.[37]

In a previous paper we showed that the photoconductivity of P3HT/$Zn_{1-x}Mg_xO$ correlates well with the electron mobility in the oxide layer, which is not observed here.[27] In particular, the results of P3HT/ZnO nanorod composites are the same without annealing and after annealing at 150°C, while the bare ZnO nanorods show a ~ 2 fold increase with the 150°C annealing. In the P3HT/$Zn_{1-x}Mg_xO$ work, the only parameter that changed between samples was the electron mobility in the oxide caused by Mg alloying. However, in the present system annealing could cause multiple changes in the composite: the mobility of electrons in ZnO, the structure and transport properties of the polymer, as well as the surface area of contact between the oxide and the polymer. For example, the increase in surface area and electron mobility in the ZnO with 225 °C annealing are expected to have a beneficial effect on the photoconductivity, but the annealing step could have a negative effect of decreasing the carrier mobility in the polymer thereby partially reducing the expected overall increase. In addition, the increase in the ZnO electron mobility might be different in the composites where the ZnO is capped with the P3HT from in bare nanorod arrays. Therefore, it is currently not definitive to identify the primary cause of the increase in photoconductivity of the composite annealed at 225 °C.

Conclusions

In conclusion, we have demonstrated that polymer processing has a strong effect on P3HT/ZnO nanorod photovoltaic device performance. We showed that using dichlorobenzene as the solvent led to enhanced infiltration, polymer order, and device performance when compared to chloroform in as-prepared devices. In addition, the infiltration of the P3HT into the ZnO nanorod array and device characteristics were both improved through annealing. Melting P3HT at 225 °C also increased the TRMC signal in the composite films, where the signal in both the individual materials increased as well. The device performance was shown to increase with enhanced infiltration, and devices that had been slow cooled from at melt at 225 °C has demonstrated a power conversion efficiency of 0.28%, a V_{OC} of 440 mV, a J_{SC} of 1.33 mA/cm^2, and a fill factor of 48%. In contrast to previously published results on P3HT infiltrated into mesoporous TiO_2, we found that EQE increases with increasing amount of polymer embedded in the ZnO nanorod arrays. The difference in the two systems can be attributed to the larger pore size and vertical order in the ZnO nanorod arrays. Thus, these data clearly show that the optimization of solvent selection and polymer processing can significantly improve the performance of P3HT/ZnO nanorod composite devices.

References

Coakley, K. M.; McGehee, M. D. *Appl. Phys. Lett.* **2003**, *83*, 3380.

Shaheen, S. E.; Ginley, D. S.; Jabbour, G. E. *MRS Bull.* **2005**, *30*, 10.

Brabec, C. J.; Hauch, J.; Choulis, S.; Schilinsky, P.; Zeira, E.; Sokolik, I. Challenges in Flexible Organic Phovoltaics. In *Organic and Nanoparticle Hybrid Photovoltaic Devices, MRS Spring Meeting*; Materials Research Society: San Francisco, 2007.

Kim, Y.; Cook, S.; Tuladhar, S. M.; Choulis, S. A.; Nelson, J.; Durrant, J. R.; Bradley, D. D. C.; Giles, M.; McCulloch, I.; Ha, C.-S.; Ree, M. *Nature Mater.* **2006**, *5*, 197.

Li, G.; Shrotriya, V.; Huang, J.; Yao, Y.; Moriarty, T.; Emery, K.; Yang, Y. *Nature Mater.* **2005**, *4*, 864.

Ma, W.; Yang, C.; Gong, X.; Lee, K.; Heeger, A. J. *Adv. Funct. Mater.* **2005**, *15*, 1617.

Padinger, F.; Rittberger, R. S.; Sariciftci, N. S. *Adv. Funct. Mater.* **2003**, *13*, 85.

Shaheen, S. E.; Brabec, C. J.; Sariciftci, N. S.; Padinger, F.; Fromherz, T.; Hummelen, J. C. *Appl. Phys. Lett.* **2001**, *78*, 841.

Schilinsky, P.; Waldauf, C.; Brabec, C. J. *Adv. Funct. Mater.* **2006**, *16*, 1669.

Shaheen, S. E.; Radspinner, R.; Peyghambarian, N.; Jabbour, G. E. *Appl. Phys. Lett.* **2001**, *79*, 2996.

Beek, W. J. E.; Wienk, M. M.; Janssen, R. A. J. *Adv. Mater.* **2004**, *16*, 1009.

Beek, W. J. E.; Wienk, M. M.; Janssen, R. A. J. *Adv. Funct. Mater.* **2006**, *16*, 1112.

Beek, W. J. E.; Wienk, M. M.; Kemerink, M.; Yang, X.; Janssen, R. A. J. *J. Phys. Chem. B* **2005**, *109*, 9505.

Coakley, K. M.; Liu, Y.; Goh, C.; McGehee, M. D. *MRS Bull.* **2005**, *30*, 37.

Coakley, K. M.; McGehee, M. D. *Chem. Mater.* **2004**, *16*, 4533.

Coakley, K. M.; Srinivasan, B. S.; Ziebarth, J. M.; Goh, C.; Liu, Y.; McGehee, M. D. *Adv. Funct. Mater.* **2005**, *15*, 1927.

Halls, J. J. M.; Pichler, K.; Friend, R. H.; Moratti, S. C.; Holmes, A. B. *Appl. Phys. Lett.* **1996**, *68*, 3120.

Kroeze, J. E.; Savenije, T. J.; Vermeulen, M. J. W.; Warman, J. M. *J. Phys. Chem. B* **2003**, *107*, 7696.

Lewis, A. J.; Ruseckas, A.; Gaudin, O. P. M.; Webster, G. R.; Burn, P. L.; Samuel, I. D. W. *Org. Elect.* **2006**, *7*, 452.

Olson, D. C.; Piris, J.; Collins, R. T.; Shaheen, S. E.; Ginley, D. S. *Thin Solid Films* **2006**, *496*, 26.

Olson, D. C.; Shaheen, S. E.; Collins, R. T.; Ginley, D. S. *J. Phys. Chem. C* **2007**, In press.

Peiró, A. M.; Ravirajan, P.; Govender, K.; Boyle, D. S.; O'Brien, P.; Bradley, D. D. C.; Nelson, J.; Durrant, J. R. *J. Mater. Chem.* **2006**, *16*, 2088.

Ravirajan, P.; Peiro, A. M.; Nazeeruddin, M. K.; Graetzel, M.; Bradley, D. D. C.; Durrant, J. R.; Nelson, J. *J. Phys. Chem. B* **2006**, *110*, 7635.

Lee, Y.-J.; Sounart, T. L.; Scrymgeour, D. A.; Voigt, J. A.; Hsu, J. W. P. *J. Cryst. Growth* **2007**, *304*, 80.

Greene, L. E.; Law, M.; Tan, D. H.; Montano, M.; Goldberger, J.; Somorjai, G.; Yang, P. *Nano Letters* **2005**, *5*, 1231.

Kroeze, J. E.; Savenije, T. J.; Warman, J. M. *J. Am. Chem. Soc.* **2004**, *126*, 7608.

Piris, J.; Kopidakis, N.; Olson, D. C.; Shaheen, S. E.; Ginley, D. S.; Rumbles, G. *Adv. Funct. Mater.* **2007**, submitted.

Dicker, G.; Haas, M. P. d.; Siebbeles, L. D. A.; Warman, J. M. *Phys. Rev. B* **2004**, *70*, 045203.

Li, G.; Yao, Y.; Yang, H.; Shrotriya, V.; Yang, G.; Yang, Y. *Adv. Funct. Mater.* **2007**, *17*, 1636.

Coakley, K. M.; Liu, Y.; McGehee, M. D.; Frindell, K. L.; Stucky, G. D. *Adv. Funct. Mater.* **2003**, *13*, 301.

Wang, G.; Swensen, J.; Moses, D.; Heeger, A. J. *J. Appl. Phys.* **2003**, *93*, 6137.

Cho, S.; Lee, K.; Yuen, J.; Wang, G.; Moses, D.; Heeger, A. J.; Surin, M.; Lazzaroni, R. *J. Appl. Phys.* **2006**, *100*, 114503.

Bao, Z.; Dodabalapur, A.; Lovinger, A. J. *Appl. Phys. Lett.* **1996**, *69*, 4108.

Govender, K.; Boyle, D. S.; Kenway, P. B.; O'Brien, P. *J. Mater. Chem.* **2004**, *14*, 2575.

Peterson, R. B.; Fields, C. L.; Gregg, B. *Langmuir* **2004**, *20*, 5114.

Quist, P. A. C.; Beek, W. J. E.; Wienk, M. M.; Janssen, R. A. J.; Savenije, T. J.; Siebbeles, L. D. A. *J. Phys. Chem. B* **2006**, *110*, 10315.

Baxter, J. B.; Schmuttenmaer, C. A. *J. Phys. Chem. B* **2006**, *110*, 25229.

Effect of ZnO processing on the photovoltage of ZnO / poly(3-hexylthiophene) solar cells

Introduction

Photovoltaic devices based on nanostructured organic/inorganic composites promise low-cost solar energy production.[1] Such devices rely on electron transfer from the conjugated polymer to the inorganic electron acceptor. Hence, the band alignment and surface chemistry across the polymer-inorganic interface is critically important. In particular, the photovoltage at open circuit (V_{OC}) is determined by the interfacial band alignment.[2-4] Since the true band alignment at the interface is difficult to obtain, the theoretical V_{OC} is calculated using bulk band structures of the two materials. Experimentally, the V_{OC} is often found to be significantly smaller than the theoretical value.[5,6] In addition, a wide range of V_{OC} and device performance were reported on hybrid polymer-ZnO nanorod composite devices.[7-11] In this study, we report on the sensitivity of ZnO surface treatments prior to polymer infiltration deposition on interfacial dipoles, the band alignment, and the resultant device performance. This is the first work that focuses on interfacial processing effects on polymer/ZnO devices and provides insight into the varying results in the literature.

Materials and Methods

Sample Preparation. Devices were fabricated on patterned indium tin oxide (ITO) coated glass substrates. Planar ZnO films were fabricated by spin coating from a 2-methoxyethanol solution containing 0.75 M zinc acetate and 0.75 M ethanol amine. The sol-gel film was subsequently annealed on a hot plate in air at 300 °C for 10 minutes. For ZnO nanorod devices, ZnO nanorods were grown from a seed layer in a solution containing 25 mM zinc nitrate and 25 mM hexamethylenetetramine at 92.5°C for 75 minutes.[12,13] The resulting ZnO nanorods were 200 nm in length and 45 nm in diameter. Poly(3-hexylthiophene) (P3HT) was used as purchased from Rieke Metals. P3HT films were deposited on top of ZnO films or nanorods by spin coating from a 1,2-dichlorobenzene solution and dried slowly over the course of 45 minutes. No additional treatments were performed on P3HT/ZnO bilayer samples. The P3HT/ZnO nanorod composites were subsequently heated at 150 °C for 10 minutes in an N_2 atmosphere to enhance polymer infiltration.[14] Finally, silver electrodes (100 nm) were thermally evaporated to make devices with areas of 0.1 cm^2.

Sample Characterization. UV-vis absorption spectra were measured using an Ocean Optics, Inc. USB-ISS-UV/VIS with a USB 2000 spectrometer. Contact angle measurements of de-ionized water on the treated surfaces were performed using a Krüss DSA1. Kelvin probe measurements were performed in air using a Monroe Electronics Isoprobe Electrostatic Voltmeter, model 244A with a model 1017AS probe. X-ray diffraction data were collected on a Bruker D-8. The morphology of the ZnO nanorods and the P3HT/ZnO nanorod composites was characterized using a Zeiss field-emission source scanning electron microscope (SEM). The samples were prepared for cross-sectional SEM by scoring the substrate, cooling them in liquid nitrogen, and cleaving the cold substrates to obtain a clear cross-section. The current density-voltage (*J*-*V*) response of the devices was measured with a Keithley 238 high current source power meter on a Spectrolab XT-10 solar simulator, which was calibrated for AM1.5

illumination with a light intensity of 100 mW/cm^2 using a reference Si solar cell and was corrected for spectral mismatch. Light intensity dependent *J-V* measurements were performed using neutral density filters. The external quantum efficiency (EQE) spectra were measured using a calibrated Si photodiode with a spot size smaller than the device area and an intensity of 2 μW at 520 nm. The photoconductivity of the polymer, nanorods, and composites were measured using the contactless time-resolved microwave conductivity (TRMC) technique. In TRMC measurements, the ZnO/P3HT bilayers were excited with a laser fluence of 2 mJ/cm^2/pulse at 532 nm. The transient change of the microwave power in the cavity, ΔG, due to transient changes in the conductance of the sample was monitored with nanosecond resolution.[14,16] Details of TRMC measurements have been published previously.[14-17]

Results and Discussion

We found that the surface properties of ZnO, as measured by contact angle or Kelvin probe, depend strongly on its processing history, e.g. whether and what solvent was used to rinse the sample and how long it was exposed to ambient. In order to establish a reproducible procedure, immediately prior to depositing the polymer, the ZnO films were treated one of two ways: (A) treating with UV/ozone for 20 minutes, or (B) heating on a hotplate at 150 °C in air for 20 minutes followed by cooling under flowing N_2. The performance of devices without any surface treatment varies widely due to the sensitivity of the ZnO to processing history. The two treatments demonstrated reproducible device results and were chosen because (A) UV/ozone is commonly used to remove hydrocarbon contamination, and (B) mild heating helps remove physisorbed water molecules.

The effects of different treatments on the ZnO properties were examined by contact angle and Kelvin probe measurements. Ozone treatment produced a very hydrophilic surface with near zero degree contact angle for water, consistent with removal of hydrocarbon. Measurements were performed in air relative to the untreated ITO substrates. These values are a measure of a relative change in contact potential difference (CPD), i.e. the Fermi level position or work function. UV/ozone treatment (treatment A) of the planar ZnO sol-gel films resulted in an increase of 0.4 ± 0.1 V (further from vacuum) in the CPD compared to the films that were heated at 150 °C in air (treatment B). The same 0.4 ± 0.1 V difference was found in ZnO nanorod films. In addition, preliminary ultraviolet photoemission (UPS) study also shows an increased work function of ZnO nanorods after ozone treatment.[18] Furthermore, there was no observed difference on P3HT wetting or infiltration into ZnO nanorod arrays as inferred from cross-sectional scanning electron microscope images. UV-vis absorption spectra of the P3HT films indicated that there was no observable difference in the polymer crystallinity at the ZnO interface for the two treatments.

	V_{OC} (mV)	J_{SC} (mA/cm^2)	*FF* (%)	η (%)
UV/O_3 bilayer	144	0.41	36	0.02
150°C bilayer	371	0.52	49	0.09
UV/O_3 rods	243	1.02	43	0.11
150°C rods	438	1.24	47	0.25

Table 1. Photovoltaic performance of the treated bilayer and ZnO nanorod devices, open circuit voltage (V_{OC}), short circuit current density (J_{SC}), fill factor (FF), power conversion efficiency (η).

In contrast, the photovoltaic device performance of the P3HT/ZnO was found to strongly depend on the ZnO treatment. The current density - voltage (J-V) response of the devices was measured on a solar simulator. Figure 1 shows the AM1.5 J-V characteristics of P3HT/ZnO bilayer devices fabricated with the two different treatments prior to P3HT deposition. Generally, the devices that were treated with UV/ozone (treatment A) displayed inferior performance. Most notably, the V_{OC} was ~ 230 mV lower when ZnO films were treated with UV/ozone compared to those heated at 150 °C (Table 1). Additionally, the short circuit current density (J_{SC}) was ~ 20% lower in the ozone treated device, which could be the result of poor contact between the polymer and the ZnO surface. Similar effects of ZnO processing were observed in ZnO nanorod devices as seen in Table 1. Note that for a given treatment, the V_{OC} of the nanorod devices is ~100 mV higher than the corresponding ZnO film devices. This is consistent with the CPD of the rods being nearly 0.1 V smaller than the planar sol-gel ZnO films of the same treatment. In addition, the dark J-V of ozone treated devices (Fig. 1 inset) demonstrated a less ideal diode behavior and higher reverse bias leakage. The V_{OC} value achieved for the ZnO nanorod device heated at 150°C (438 mV) is comparable to our previous results on ZnO nanorod devices heated at 200 °C prior to polymer deposition (440 mV).[7,8]

The V_{OC} after heating at 150°C in air is significantly higher than values reported by other groups where the treatments of ZnO were different. In Refs. 9,10, the V_{OC} was found to be < 100 mV when the ZnO rods were soaked in dilute P3HT, and ~ 250 mV when the ZnO rods were exposed to ruthenium dye solutions. In Ref. 11, the V_{OC} was reported to be 170 mV with ZnO rods that had been exposed to dilute HCl, subsequently annealed for 10 minutes in air at 200 °C, and finally exposed to low oxygen partial pressures in an argon glove box. Fabrication of P3HT/ZnO devices in an argon glove box has previously been shown to dramatically reduce the V_{OC}.[8,19-21] In light of what we found in the sensitivity of solar cell performance on the ZnO surface treatment, the large variation of the V_{OC} reported for ZnO/P3HT hybrid photovoltaics is likely due to the processing history.

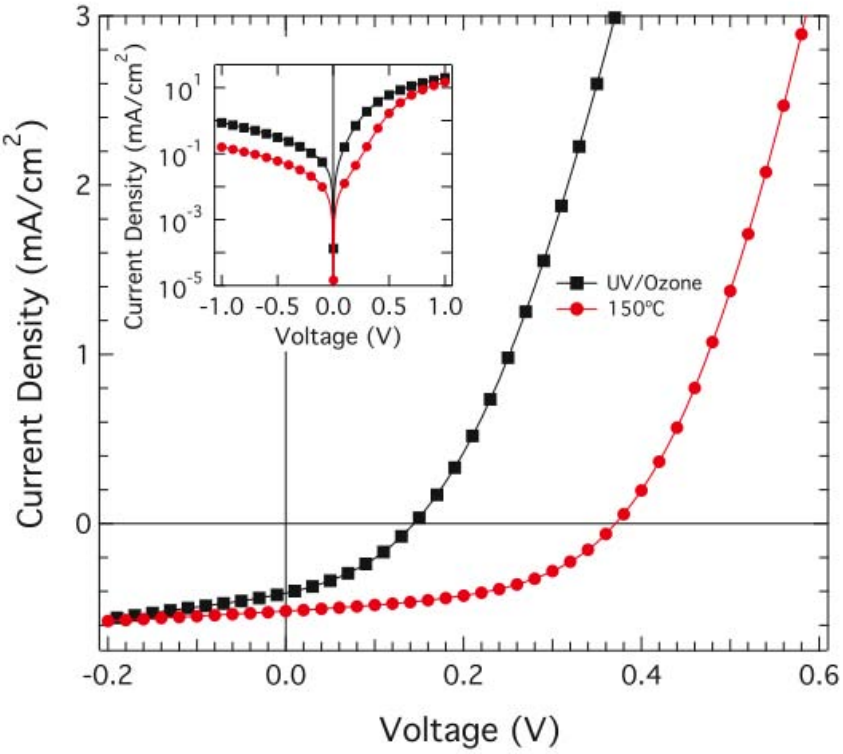

Figure 1. Current density versus voltage (J-V) for illuminated ITO/ZnO/P3HT/Ag bilayer device, ZnO treated with UV/ozone (black squares), and ZnO heated at 150 °C (red circles). Inset shows dark J-V curves.

The observed poor performance in the ozone treated ZnO devices could arise from three sources: shorting of the device, an increase in interfacial defects (traps or recombination centers), or change in band alignment between ZnO and P3HT. Since the *J-V* characteristics in the dark and under illumination are not significantly different for the two kinds of devices, we eliminate shorting as a possible cause of inferior performance due to ozone treatment. In order to help elucidate whether the predominant effect is changes in defect density or interfacial band alignment, the J_{SC} and V_{OC} were measured as a function of illumination intensity. If there were a change in the defect or trap density, one would anticipate a different dependence of the J_{SC} or V_{OC} on light intensity, since the defect density affects the relative balance between monomolecular and bimolecular recombination processes.[22] Figure 2 shows that log(J_{SC}) vs log(intensity) has a linear relationship (slope = 0.91) for both types of devices, indicating that the recombination if primarily monomolecular (slope = 1.0) with a small contribution of a bimolecular process (slope = 0.5), and that the relative contributions do not change with the ozone treatment. In addition, the V_{OC} of the two types of devices also show the same illumination dependence; in fact, the two V_{OC} curves overlap when the UV/ozone data is scaled 1.8 across all light intensities measured. Additional insight can be gained from TRMC studies.[16,23,24] TRMC data show no difference in the recombination dynamics for the two ZnO treatments (Figure 2 inset). These results strongly indicate that the interfacial defect density is not different for the two treatments, since added defects would alter the functional form of the J_{SC} and V_{OC} vs. intensity plot or carrier recombination dynamics.

Thus, the primary difference between the UV/ozone and the 150 °C anneal appears to be a change in the interfacial band alignment between P3HT and ZnO, possibly from an interfacial dipole change (Figure 3).[25,26] A change in the CPD or work function can be the result of a shift in the surface Fermi level position with respect to the band edge, or a change of surface dipole that results in rigid band shift. If the former is the dominant change from ozone treatment, a larger CPD in ozone treated surfaces would mean that the Fermi level moves towards the mid-gap (i.e. less conducting) from the n-type ZnO conduction band edge. Our preliminary UPS results support this picture.[18] However, the final band alignment between ZnO and P3HT, and hence V_{OC}, are also affected by the interfacial dipole. If we assume the interfacial dipole is not changed by the ozone treatment, shifting the Fermi level with respect to the band edge would predict a larger V_{OC} in ozone treated devices, which is opposite to the smaller observed V_{OC}. Hence, the experimental results indicate that the dominant effect of ozone treatment is a change in the interfacial dipole. Figure 3 illustrates the extreme case of the V_{OC} difference being due entirely to a change in the interfacial dipole and not at all from a shift in the Fermi level with respect to the band edge. In reality, both changes probably take place with a larger effect from the interfacial dipole.

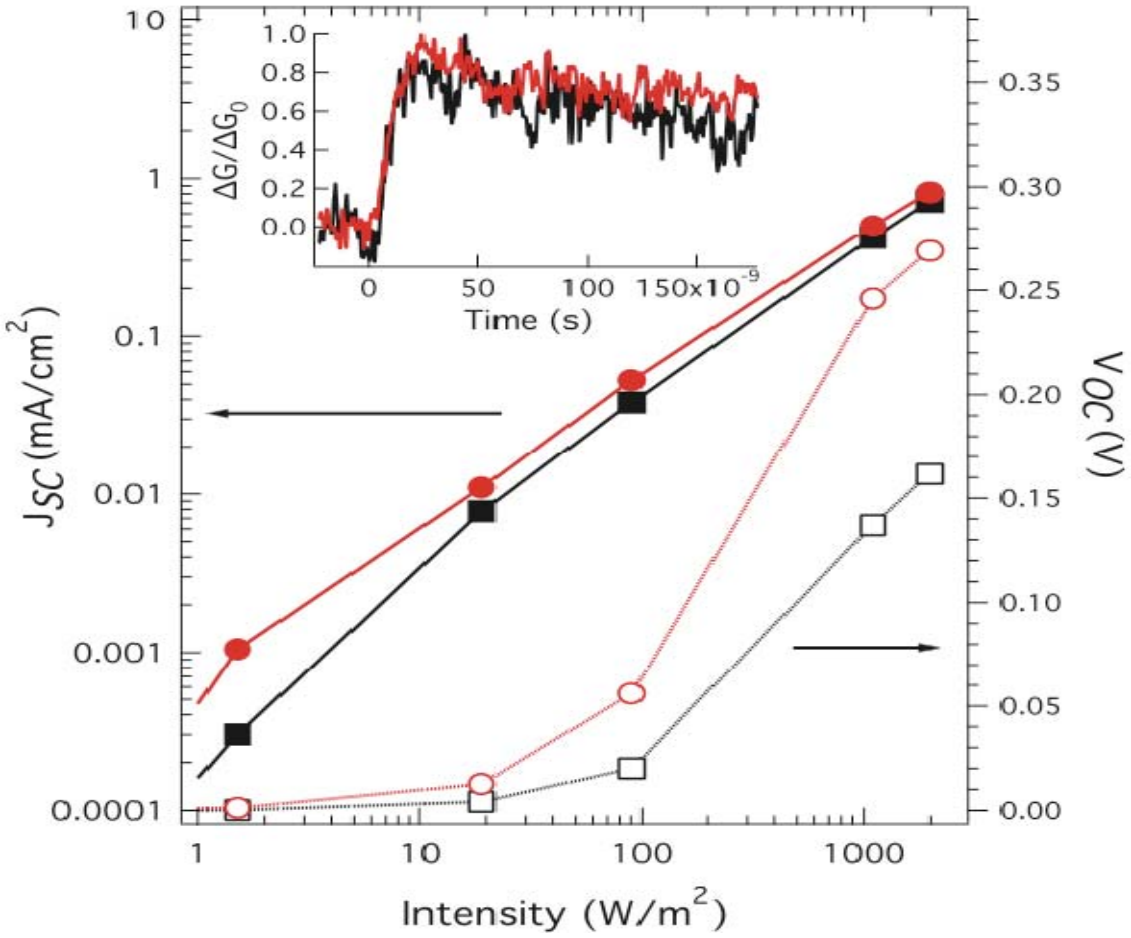

Figure 2. J_{SC} (solid symbols) and V_{OC} (open symbols) vs. illumination intensity for bilayer devices treated with UV/ozone (black squares) and heated at 150 °C (red circles). Inset shows normalized microwave conductivity transients, UV/ozone (black), 150 °C (red).

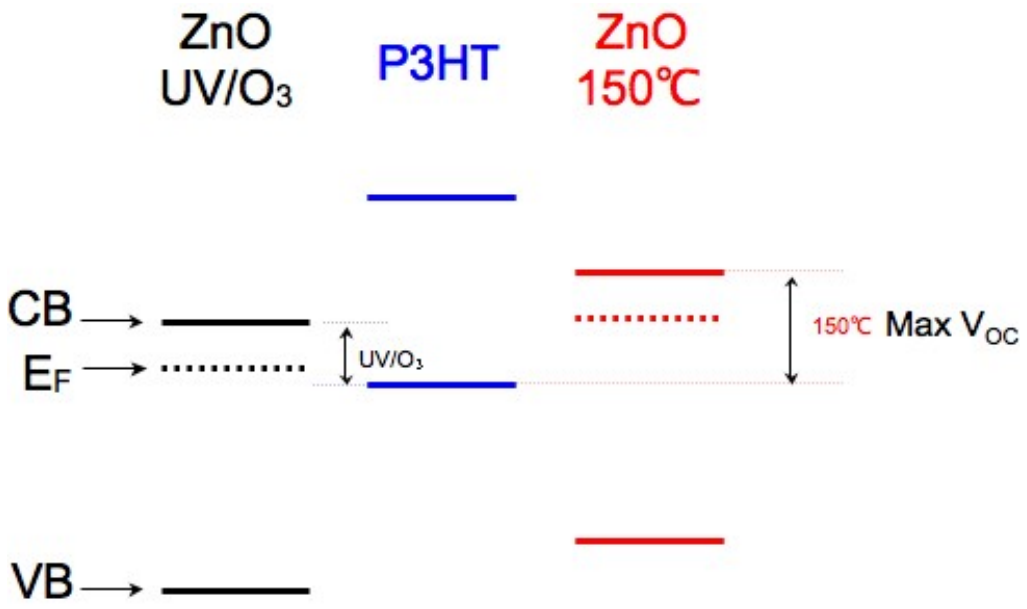

Figure 3. Band diagram for P3HT/ZnO device that illustrate the changes in interfacial dipole arising from the surface treatments: UV/ozone (black) and heated at 150 °C (red).

Conclusions

In conclusion, we have shown how ZnO surface processing prior to deposition of the polymer can dramatically affect the performance of ZnO/P3HT devices. Devices in which the ZnO films/nanorods were heated at 150 °C in air exhibited a much higher V_{OC} compared to devices with ZnO treated by UV/ozone. Based on CPD measurements of ZnO, TRMC dynamic studies of ZnO/P3HT bilayers, and intensity dependent device characterization of P3HT/ZnO devices, we conclude that the two processes result in different interfacial dipoles that cause a band alignment shift at the heterojunction interfaces. This points to intermediate materials processing as the source of the wide range of reported photovoltages for ZnO/P3HT devices. We demonstrated that moderate heating consistently produces the largest V_{OC} in P3HT/ZnO solar cells.

References

Shaheen, S. E.; Ginley, D. S.; Jabbour, G. E. *MRS Bull.* **2005**, *30*, 10.

Brabec, C. J.; Cravino, A.; Meissner, D.; Sariciftci, N. S.; Fromherz, T.; Rispens, M. T.; Sanchez, L.; Hummelen, J. C. *Adv. Funct. Mater.* **2001**, *11*, 374.

Olson, D. C.; Shaheen, S. E.; White, M. S.; Mitchell, W. J.; Hest, M. F. A. M. v.; Collins, R. T.; Ginley, D. S. *Adv. Funct. Mater.* **2007**, *17*, 264.

Rand, B. P.; Burk, D. P.; Forrest, S. R. *Phys. Rev. B* **2007**, *75*, 115327.

Mihailetchi, V. D.; Blom, P. W. M.; Hummelen, J. C.; Rispens, M. T. *J. Appl. Phys.* **2003**, *94*, 6849.

Sharber, M. C.; Mühlbacher, D.; Koppe, M.; Denk, P.; Waldauf, C.; Heeger, A. J.; Brabec, C. J. *Adv. Mater.* **2006**, *18*, 789.

Olson, D. C.; Piris, J.; Collins, R. T.; Shaheen, S. E.; Ginley, D. S. *Thin Solid Films* **2006**, *496*, 26.

Olson, D. C.; Shaheen, S. E.; Collins, R. T.; Ginley, D. S. *J. Phys. Chem. C* **2007**, *111*, 16670.

Peiró, A. M.; Ravirajan, P.; Govender, K.; Boyle, D. S.; O'Brien, P.; Bradley, D. D. C.; Nelson, J.; Durrant, J. R. *J. Mater. Chem.* **2006**, *16*, 2088.

Ravirajan, P.; Peiró, A. M.; Nazeeruddin, M. K.; Graetzel, M.; Bradley, D. D. C.; Durrant, J. R.; Nelson, J. *J. Phys. Chem. B* **2006**, *110*, 7635.

Greene, L. E.; Law, M.; Yuhas, B. D.; Yang, P. *J. Phys. Chem. C* **2007**, *111*, 18451.

Greene, L. E.; Law, M.; Tan, D. H.; Montano, M.; Goldberger, J.; Somorjai, G.; Yang, P. *Nano Lett.* **2005**, *5*, 1231.

Lee, Y.-J.; Sounart, T. L.; Scrymgeour, D. A.; Voigt, J. A.; Hsu, J. W. P. *J. Cryst. Growth* **2007**, *304*, 80.

Olson, D. C.; Lee, Y. J.; White, M. S.; Kopidakis, N.; Shaheen, S. E.; Ginley, D. S.; Voigt, J. A.; Hsu, J. W. P. *J. Phys. Chem. C* **2007**, *111*, 16640.

Kroeze, J. E.; Savenije, T. J.; Warman, J. M. *J. Am. Chem. Soc.* **2004**, *126*, 7608.

Piris, J.; Kopidakis, N.; Olson, D. C.; Shaheen, S. E.; Ginley, D. S.; Rumbles, G. *Adv. Funct. Mater.* **2007**, in press.

Savenije, T. J.; Warman, J. M.; Goossens, A. *Chem. Phys. Lett.* **1998**, *287*, 148.

Uhlrich, J. J.; Kuech, T. F.; Olson, D. C.; Hsu, J. W. P. *In Preparation*.

Lira-Cantu, M.; Krebs, F. C. *Sol. Energ. Mater. Sol. Cells* **2006**, *90*, 2076.

Lira-Cantu, M.; Norrman, K.; Andreasen, J. W.; Casan-Pastor, N.; Krebs, F. C. *J. Electochem. Soc.* **2007**, *154*, B508.

Lira-Cantu, M.; Norrman, K.; Andreasen, J. W.; Krebs, F. C. *Chem. Mater.* **2006**, *18*, 5684.

Dersch, H.; Skumanich, A.; Amer, N. M. *Phys. Rev. B* **1985**, *31*, 6913.

Kroeze, J. E.; Savenije, T. J.; Vermeulen, M. J. W.; Warman, J. M. *J. Phys. Chem. B* **2003**, *107*, 7696.

Quist, P. A. C.; Beek, W. J. E.; Wienk, M. M.; Janssen, R. A. J.; Savenije, T. J.; Siebbeles, L. D. A. *J. Phys. Chem. B* **2006**, *110*, 10315.

Cahen, D.; Kahn, A. *Adv. Mater.* **2003**, *15*, 271.

Ishii, H.; Sugiyama, K.; Ito, E.; Seki, K. *Adv. Mater.* **1999**, *11*, 605.

DISTRIBUTION

1	MS 0899	Technical Library, 9536 (electronic copy)
1	MS 0123	D. Chavez, LDRD Office, 1011 (electronic copy)
1	MS 1415	Julia Hsu, 1114 (electronic copy)
1	MS 1415	Carlos Gutierrez, 1114 (electronic copy)
1	MS 1411	Jim Voigt, 1816 (electronic copy)

Sandia National Laboratories